

## RADIO BRIDGE STRUCTURE AND ITS APPLICATION TO ESTIMATE THE MACH NUMBER AND AMBIENT GAS TEMPERATURE OF POWERFUL SOURCES

GREG F. WELLMAN, RUTH A. DALY,<sup>1</sup> AND LIN WAN

Department of Physics, Princeton University, Princeton, NJ 08544-0708

*Received 1996 July 31; accepted 1996 November 22*

### ABSTRACT

The radio bridge shape of very powerful extended (FR II) radio sources has been studied in detail; the sample used here includes 12 radio galaxies and six radio-loud quasars with redshifts between 0 and 1.8. Specifically, the width and radio surface brightness of the radio bridge are measured as a function of distance from the radio hot spot on each side of each source.

The width as a function of distance from the hot spot agrees very well with theoretical predictions based on the standard model of bridge growth, in which the bridge expands laterally because of a blast wave driven by the large pressure difference between the relativistic plasma in the radio hot spot and surrounding radio lobe and the adjacent ambient gas. The simple assumptions that go into the theoretical prediction are that the lobe radio power and width (measured in the vicinity of the radio hot spot) are roughly constant over the lifetime of a given source, and that the rate at which the bridge lengthens, referred to as the lobe propagation velocity, is roughly constant over the lifetime of a source. These three assumptions appear to be consistent with other independent studies of very powerful extended radio sources of the type studied here, within the present (rather large) observational uncertainties.

The radio surface brightness as a function of distance from the hot spot agrees surprisingly well with a simple model in which the radio bridge undergoes adiabatic expansion in the lateral direction, assuming that the initial lobe radio power and lobe width are time independent for a given source. That is, the observed lobe surface brightness and width, and the width as a function of position along the radio bridge, are used to predict the radio surface brightness as a function of position along the radio bridge, assuming adiabatic expansion of the bridge in the lateral direction. The predicted and observed surface brightness along the bridge agree surprisingly well. This suggests that there is little reacceleration of relativistic electrons within the radio bridge and that the backflow velocity of relativistic plasma within the bridge is small compared with the lobe advance velocity. These results are consistent with implications based on the bridge shape and structure discussed by Alexander & Leahy since we consider only very powerful FR II sources here.

The Mach number with which the radio lobe propagates into the ambient medium can be estimated using the structure of the radio bridge; this Mach number is the ratio of the lobe propagation velocity to the sound speed of the ambient gas. The lateral expansion of the bridge is driven initially by a blast wave. When the velocity of the blast wave falls to a value of the order of the sound speed of the ambient medium, the character of the expansion changes, and the functional form of the bridge width as a function of position exhibits a break, which may be used to estimate the ratio of the lobe advance velocity to the sound speed of the ambient gas. We observe this break in several sources studied here. The Mach number of lobe advance depends only upon the ratio of the width to the length of the bridge as a function of position, which is purely geometric. Typical Mach numbers obtained range from about 2 to 10 and seem to be roughly independent of redshift and the total size (core-lobe separation) of the radio source.

The Mach number can be used to estimate the temperature of the ambient gas if an independent estimate of the lobe propagation velocity is available. Lobe propagation velocities estimated using the effects of synchrotron and inverse Compton aging of the relativistic electrons that produce the radio emission are combined with the Mach numbers in order to estimate ambient gas temperatures. The temperature obtained for Cygnus A matches that indicated by X-ray data for this source. Typical temperatures obtained range from about 1 to 20 keV. This temperature is characteristic of gas in clusters of galaxies at low redshift, which is interesting since we show in a companion paper that the ambient gas density in the vicinity of the same sources is similar to that observed in low-redshift clusters of galaxies.

The temperature and density estimates of the ambient gas in the vicinity of any given source are combined to estimate the cooling time of the gas, which indicates whether or not the source is likely to be in a cooling flow region. It does appear that many of the sources may be in regions that would be defined as “cooling flow regions,” since, for many sources, the cooling time is less than the age of the universe at the redshift of the source.

It has been pointed out by Carilli et al. that the magnetic field strength in Cygnus A is likely to be about 0.3 of the minimum-energy value. We repeat the two independent tests discussed by Carilli et al. for Cygnus A and add a third independent test. All three tests suggest an offset from equipartition or

<sup>1</sup> National Young Investigator.

minimum-energy conditions that are consistent with the Carilli et al. result; we obtain an offset of about 0.25. Furthermore, it is shown in a companion paper that all sources are likely to have a similar offset; the source-to-source dispersion in the offset must be less than about 15%.

*Subject headings:* cooling flows — cosmology: observations — galaxies: active — galaxies: clusters: general — shock waves

## 1. INTRODUCTION

In the standard “beam model” of FR II radio sources (e.g., Begelman, Blandford, & Rees 1984 and references therein), the active galactic nucleus (AGN) emits two collimated beams in opposite directions. Each beam powers a driven shock wave through the ambient medium and deposits its energy as relativistic electrons and magnetic field behind the shock. The electrons then spiral about the magnetic field emitting synchrotron radiation. The shocked jet material behind the hot spot inflates a cocoon around the beam, and the shocked ambient medium forms a sheath (outer cocoon) around the inner cocoon. In the part of the bridge near the radio hot spot, both inner and outer cocoons are believed to be overpressured with respect to the ambient, unshocked, medium (e.g., Begelman & Cioffi 1989; Daly 1990).

A strongly overpressured region expands and drives a shock wave into the ambient gas. Begelman & Cioffi (1989) and Daly (1990) discuss forms for the expansion. Synchrotron emission is thought to be produced by the shocked jet material only, so lateral expansion of the radio bridge is expansion of the inner cocoon and does not necessarily measure the expansion of the outer cocoon. The outer cocoon boundary may be indicated by a discontinuity in the rotation measure as observed for the bow shock region of Cygnus A (Carilli, Perley, & Dreher 1988).

In this paper, the width and surface brightness of the radio bridge are measured at several positions along the bridge for each of a sample of very powerful ( $P_{178} > 10^{27} h^{-2} \text{ W Hz}^{-1} \text{ sr}^{-1}$ ) FR II radio sources. The width measurements are used to generate a composite expansion profile, which agrees with theoretical predictions surprisingly well. The surface brightness and width measurements are used to compare the predicted and observed surface brightness as a function of position, assuming adiabatic expansion of the bridge, and a lobe surface brightness and width that are time-independent for any given source. The predicted and observed surface brightnesses agree very well, indicating there is little reacceleration of relativistic electrons and insignificant backflow of relativistic plasma within the radio bridge.

In some sources, a break is seen in the bridge width as a function of position relative to the radio hot spot. This is interpreted as the transition region where the lateral expansion of the bridge becomes sonic. The characteristics of the break are used to estimate of the Mach number of lobe advance. The estimate of the Mach number is then combined with the lobe advance velocity, which is estimated using synchrotron and inverse Compton aging, in order to estimate the sound speed, and hence temperature, of the ambient gas in the vicinity of the radio source.

The paper is structured as follows. The basic assumptions are discussed in § 2, and the relation between adiabatic lateral expansion and surface brightness is given in § 3. The sample is described in § 4, and the data analysis and deconvolution procedure in § 5. Results are presented in § 6, with the bridge widths as a function of distance from the hot spot discussed in § 6.1, the observed surface brightnesses dis-

cussed in § 6.2, and the observed surface brightnesses compared with those predicted by adiabatic lateral expansion in § 6.3. More detailed source physics and the blast-wave model are presented in § 7. Applications of the theory to the data are presented in § 8, with Mach numbers of the lobe advance given in § 8.1, ambient temperature estimates discussed in § 8.2, and cooling time estimates presented in § 8.3. A discussion of the ratio of the true magnetic field strength to the minimum-energy magnetic field is given in § 8.2.1. Three independent estimates of this ratio are presented and found to be in reasonable agreement. The effects of the cosmological parameters chosen are discussed in § 9. A summary and conclusions follow in § 10.

Hubble’s constant is taken to be  $H_0 = 100 h \text{ km s}^{-1} \text{ Mpc}^{-1}$ , the cosmological constant is assumed to be zero, and the deceleration parameter is taken to be  $q_0 = 0$  throughout the paper, except in § 9 where  $q_0 = 0.5$  is discussed.

## 2. BASIC ASSUMPTIONS

At 178 MHz radio powers greater than about  $10^{26}$ – $10^{27} h^{-2} \text{ W Hz}^{-1} \text{ sr}^{-1}$ , radio sources have a fairly straight, regular bridge implying little or no backflow (e.g., Leahy & Williams 1984; Alexander & Leahy 1987). The sources used in this study have  $P_{178} > 10^{27} h^{-2} \text{ W Hz}^{-1} \text{ sr}^{-1}$ , and the bridges all appear to be regular in shape. Only very powerful extended sources are included in this study, so that it will be likely that the lateral expansion of the radio bridge is driven predominantly by a blast wave (discussed in more detail in § 7) rather than driven by backflow. Recent work by Scheuer (1995, 1996) on the asymmetry of powerful extended radio sources and implications for backflow for the sample considered here are discussed in detail in § 10, where it is concluded that little backflow and the observed arm-length asymmetries are consistent with typical lobe propagation velocities estimated here.

It is assumed here that the bridge material in high-power radio sources can be modeled as quiescent (i.e., undergoing negligible reacceleration of relativistic electrons) and that the bridge is cylindrically symmetric some distance behind the hot spot toward the radio core. Following Carilli et al. (1991) and Leahy (1991), it is assumed that the magnetic field is tangled in three dimensions and that the volume emissivity is constant within a given cross-sectional slice at a fixed position  $x$  from the radio hot spot. Deviation from these assumptions may be significant close to the hot spot; for example, the lobe/hot spot region of Cygnus A is observed to have a complex structure of primary and secondary hot spots, collimated flows, and turbulence (Perley & Carilli 1996; Carilli et al. 1996). However, the approximation is likely a good one a sufficient distance behind the hot spot, where the age of the synchrotron plasma is a few sound crossing times. This constant emissivity cross section model has the following simple form for the surface brightness  $S$  through the cross section (prior to convolution with the beam):

$$S(x, y) = S(x, 0) \sqrt{1 - \left[ \frac{y}{a(x)} \right]^2}, \quad (1)$$

where  $x$  is the distance from the hot spot along the hot spot–core axis,  $y$  is the projected height from that axis, and  $a(x)$  is the bridge half-width. Given this form for the surface brightness, the surface brightness along the bridge axis,  $S(x, 0)$ , and bridge half-width,  $a(x)$ , that is a distance  $x$  from the radio hot spot can be deduced after accounting for convolution with the beam used to observe the source, yielding the “observed” surface brightness and half-width as a function of position along the bridge.

High polarization has been observed in some parts of some sources such as Cygnus A (Perley & Carilli 1996), which can be explained by anisotropic magnetic field models such as those suggested by Laing (1980, 1981). Such models may be rather complicated. Adiabatic cooling in these models tends to move the magnetic field and relativistic particles away from equilibrium (Blandford 1996). Moreover, factors such as magnetic stress and pressure gradients in the lobe will probably cause hydromagnetic waves or magnetic reconnection to be important, further complicating the problem (e.g., Blandford 1996).

The radio polarization properties of many extended powerful radio sources have been studied by different authors who reported low or moderate degrees of polarization in the radio bridge, which is the region that is relevant in the study presented here (e.g., Garrington, Conway, & Leahy 1991; Fernini et al. 1993). For example, the percentage polarization in the bridges of six of the sources studied here (3C 55, 3C 265, 3C 270.1, 3C 275.1, 3C 334, and 3C 256) are typically below 10%. Thus, while anisotropic magnetic fields might be present in some regions of some sources, notably the boundary region around the radio hot spot and lobe, it is likely that the tangled  $B$ -field model provides a good, rough approximation in the radio bridges of the sources studied here.

If the magnetic fields in the radio bridges of the sources studied here are not tangled in three dimensions but are anisotropic, as suggested by Laing (1980, 1981), then the functional forms derived here hold, but the normalization may change. For example, the lateral surface brightness profile (i.e., the profile perpendicular to the radio axis) prior to convolution with a Gaussian beam is somewhat different for models with anisotropic magnetic fields than it is for those with tangled fields. Usually, the surface brightness profile across the bridge in anisotropic models is more peaked in the center of the radio bridge. Specifically, the FWHM of the lateral surface brightness profile in Laing’s model “C” (Laing 1981) is about 28% narrower prior to convolution with a Gaussian beam than that in the constant emissivity model assumed here. Assuming a lateral intensity profile such as Laing’s model “C” will not affect any of the scaling relations derived here, although normalizations that depend on the intrinsic bridge width, such as the Mach number, may change slightly. Normalizations that are proportional to the bridge width, such as the Mach number, will probably only change by about 30%, comparable to the current uncertainties on this parameter.

### 3. ADIABATIC COOLING

A relation between the amount of lateral expansion [i.e.,  $a(x)$ ] and the decrease in surface brightness along the bridge [i.e.,  $S(x, 0)$ ] can be derived assuming that the lobe radius and power are roughly time-independent for a given radio source, if the lateral expansion is adiabatic, and both reacceleration of relativistic electrons and backflow of rela-

tivistic plasma are insignificant within the radio bridge. The assumption of constant lobe power over the lifetime of a given source is consistent with the absence of an observable correlation between source length and power for sources of the type considered here (Neuser et al. 1995). Following Pacholczyk (1970), let us consider a volume  $V$  containing  $N_{\text{tot}}$  relativistic electrons with a power-law energy distribution written in terms of the Lorentz factor,  $\gamma$ ,  $n(\gamma)d\gamma = n\gamma^{-s}d\gamma$  from  $\gamma = \gamma_{\text{co}}$ , the low-energy cutoff, to  $\infty$ , so

$$N_{\text{tot}} = nV \int_{\gamma_{\text{co}}}^{\infty} \gamma^{-s} d\gamma = nV\gamma_{\text{co}}^{-2\alpha}/2\alpha, \quad (2)$$

where  $\alpha = (s - 1)/2$  is the radio spectral index. The radio power from this region is

$$P_v = \left( \frac{4\pi e^3}{9m_e c^2} \right) nVE^{-2\alpha}B_{\perp}, \quad (3)$$

where  $E = \gamma m_e c^2$  is the electron energy,  $m_e$  is the rest mass of the electron,  $c$  is the speed of light,  $e$  is the electron charge, and the relation between the frequency of emission,  $\nu$ , and  $E$  is

$$\nu = \frac{3eB_{\perp}}{4\pi m_e c} \left( \frac{E}{m_e c^2} \right)^2, \quad (4)$$

where  $B_{\perp}$  is the component of the magnetic field perpendicular to the electron motion. For a tangled field,  $B_{\perp}^2 = (2/3)B^2$ .

Following Moffet (1975) and Daly (1992), the cylindrical expansion of a slice of a bridge with initial half-width  $a_0$  to half-width  $a$  causes the following changes to occur:

$$\gamma = (a/a_0)^{-2/3}\gamma_0, \quad (5)$$

$$B = (a/a_0)^{-4/3}B_0, \quad (6)$$

and

$$V = (a/a_0)^2 V_0, \quad (7)$$

where the expansion is assumed to be adiabatic; note that a subscript zero refers to quantities prior to expansion and those lacking the subscript zero refer to quantities after expansion. For constant observing frequency  $\nu$ , equations (4) and (6) imply that  $E = (a/a_0)^{2/3}E_0$ . Equations (2) and (5) imply that  $nV = (a/a_0)^{-4\alpha/3}n_0V_0$ . Substituting these powers of  $(a/a_0)$  into equation (3) gives the result that

$$P_v = (a/a_0)^{-8\alpha/3-4/3}P_{v,0}. \quad (8)$$

Hence, the volume emissivity varies as  $\varepsilon_v = (a/a_0)^{-8\alpha/3-10/3}\varepsilon_{v,0}$ , and the surface brightness of a point following the expansion varies as

$$S_v = (a/a_0)^{-8\alpha/3-7/3}S_{v,0}. \quad (9)$$

For comparison, in the case of spherical expansion, the power in equation (9) would be  $-4\alpha - 4$ .

### 4. THE SAMPLE

The sample used here is a subset of the sample defined by Wellman, Daly, & Wan (1997, hereafter WDW97), Wellman & Daly (1996b), and Wellman (1997); the reader is referred to WDW97 for details. In summary, the sample is drawn from the samples of two observational papers: Leahy, Muxlow, & Stevens (1989, hereafter LMS89) and Liu, Pooley, & Riley (1992, hereafter LPR92). Both groups selected sources of high radio power. LMS89 selected

sources of large angular extent, while LPR92 selected sources of small angular extent. A few sources were excluded by WDW97 because of morphological irregularities or lack of physical extent of the observable radio bridge necessary to obtain the desired data, leaving 41 lobes from 22 sources in Wellman & Daly (1996b) and WDW97.

In this paper, a few more lobes were excluded because of difficulty obtaining width measurements of sufficient number and quality, leaving 30 lobes from 18 sources. LMS89 observed at 151 MHz and 1.5 GHz. LPR92 observed at 1.5, 4.9, and 15 GHz. In general, we used the map made at the lowest available frequency so as to avoid strong effects from radiative losses (synchrotron or inverse Compton), although occasionally the second lowest was used for better resolution or lower noise. Of the 30 lobes used, measurements of 13 were taken from 151 MHz maps, 15 from 1.5 GHz maps, and two from 4.9 GHz maps.

## 5. DATA ANALYSIS

Using the published maps (LMS89; LPR92), the apparent surface brightness  $S_{\text{obs}}(x, 0)$  and FWHM of the radio bridge are measured at several positions along each bridge. The positions where measurements are taken are chosen to be where surface brightness contours cross the core-hot spot ridgeline on the published maps, since, at these points, the surface brightness is known to the accuracy of the map. The model-based one-dimensional deconvolution (see § 5.1) is then applied, letting  $a(x)$  and  $S(x, 0)$  take the values that would produce the observed FWHM and  $S_{\text{obs}}(x, 0)$  after convolution with a one-dimensional Gaussian the size of the beam used to observe the source.

### 5.1. Deconvolution

The sources are not perfectly resolved, so a one-dimensional “deconvolution” was devised (WDW97) to attempt to produce a best guess for the source width and maximum surface brightness at any particular distance,  $x$ , behind the hot spot. The deconvolution is dependent on the model assumption that a radio bridge cross section is well approximated by equation (1), which is equivalent to the assumption that the bridge may be modeled as a cylinder with constant volume emissivity and half-width  $a(x)$ ; a comparison of the observed and predicted change in radio surface brightness as a function of lateral distance from the radio bridge supports this assumption. The observed  $S(x, y)$  will be equation (1) convolved with a Gaussian beam. To get the best guess for the true bridge half-width,  $a(x)$ , and maximum surface brightness,  $S(x, 0)$ , from the observed FWHM and observed maximum surface brightness, the best guess FWHM and  $S(x, 0)$  were taken to be that which, when convolved with a Gaussian of the beam size, give the observed FWHM and surface brightness. Figure 1 graphs the relations describing the deconvolution. In the left panel, the ratio of true (model) width to apparent width is given as a function of the resolution. In the right panel, the ratio of apparent  $S(x, 0)$  to true (model)  $S(x, 0)$  is given as a function of resolution. Figure 2 shows histograms of the correction factors applied to the FWHM (*left panel*) and peak surface brightness (*right panel*) for this sample. In general, after the deconvolution, the FWHM is decreased from its apparent size (by an average of 13%), and the peak surface brightness is increased (by an average of 40%) from the value obtained directly from the convolved map. The deconvolved half-width,  $a(x)$ , equals  $1/3^{1/2}$  times the deconvolved FWHM.

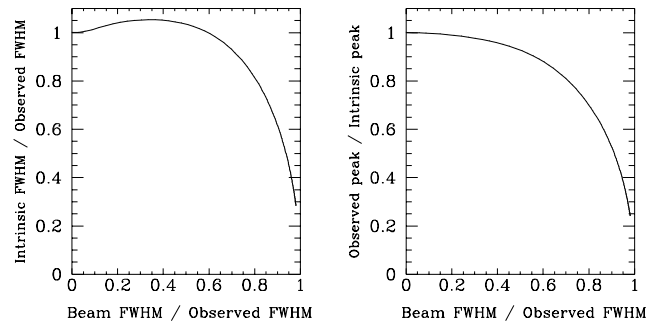


FIG. 1.—The relations describing the deconvolution. The ratios of intrinsic (model) width to observed width (*left panel*) and observed  $S(x, 0)$  to intrinsic (model)  $S(x, 0)$  (*right panel*) are given as a function of the resolution.

### 5.2. Error Analysis

The measurements of widths (FWHM) and surface brightnesses are made directly from the published maps (LMS89; LPR92) using a ruler, and the initial uncertainties in the surface brightnesses are taken to be those given therein. The initial uncertainties in the widths are estimated from the error of measurement with a ruler. The deconvolution procedure includes an increase in uncertainty as a function of how well the width of the source is resolved: the more poorly resolved, the greater the uncertainty.

## 6. EMPIRICAL RESULTS

### 6.1. Half-Width as a Function of Distance from Hot Spot

Figure 3 is a log-log composite plot of the bridge half-width,  $a$ , as a function of separation from the hot spot,  $x$ , for all 30 bridges; many sources are counted as having two bridges since the bridge on each side of a source is treated independently. There are 182 points, so there is an average of about six points for each bridge of each source. The bridge radii increase as the distance from the hot spot increases; this is interpreted as expansion of the bridge in the lateral direction. The best-fit straight line is overlaid and has a slope of  $0.492 \pm 0.005$  with a reduced  $\chi^2$  of 25.2. This agrees very well with Begelman & Cioffi (1989) and Daly (1990), who both derive relations of the form  $v_{\text{exp}} \propto t^{-1/2}$  and hence

$$a \propto x^{1/2} \quad (10)$$

for roughly time-independent lobe advance velocity  $v_L$  (see § 7 for more detail). That the reduced  $\chi^2$  is so large is not

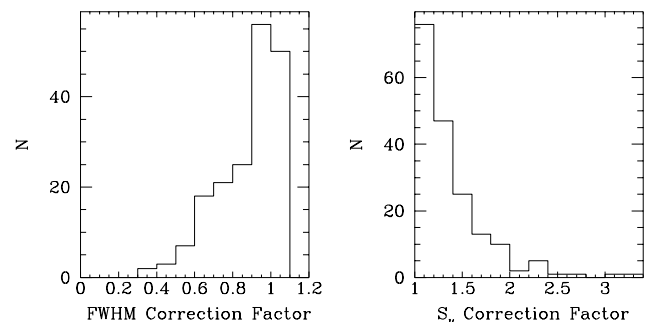


FIG. 2.—Histograms of the correction factors applied to the measured FWHMs (*left panel*) and surface brightnesses (*right panel*) as a result of the deconvolution procedure (a factor of 1 is no correction). Most corrections were small ( $< 20\%$  [*left panel*] and  $< 50\%$  [*right panel*]).

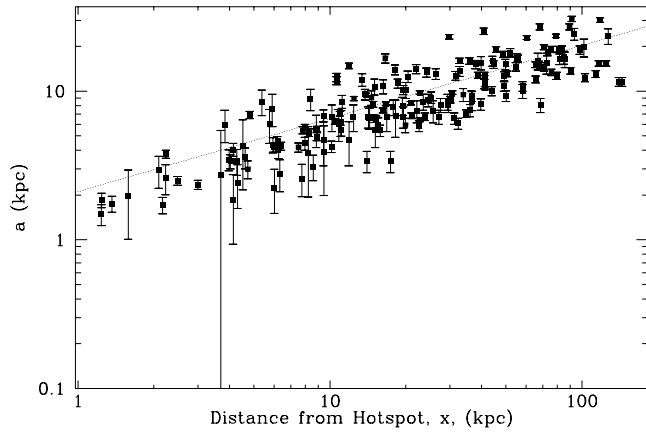


FIG. 3.—Log-log composite plot of bridge half-width as a function of separation from the hot spot for all 30 bridges. There are several points per source. The best-fit straight line is overlaid and has a slope of  $0.492 \pm 0.005$  with a reduced  $\chi^2$  of 25.2.

surprising. Each individual source only approximates equation (10), and each source may have a different constant of proportionality in that relation.

To determine the degree to which the reduced  $\chi^2$  in Figure 3 may be a result of differing constants of proportionality in equation (10), the data from each bridge are individually fitted to the form

$$a = k_L x^{1/2}, \quad (11)$$

and the constant of proportionality  $k_L$  for that lobe/bridge is estimated. Figure 4 is a log-log composite plot of normalized bridge half-width,  $a/k_L$ , as a function of separation from the hot spot,  $x$ , for all 30 bridges. The best-fit straight line is overlaid and has a slope of  $0.442 \pm 0.005$  with a reduced  $\chi^2$  of 6.8. The reduced  $\chi^2$  includes the loss of 29 degrees of freedom from using the parameters  $k_L$ . The slight decrease in the best-fit slope may indicate the presence of “breaks” in the individual expansion profiles, as predicted by the lateral expansion model discussed by Begelman & Cioffi (1989) and Daly (1990), as discussed in detail in § 7. The presence and implications of such breaks are discussed in § 8.1.

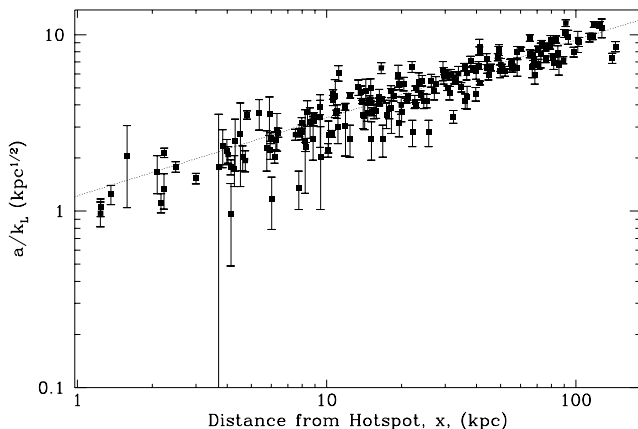


FIG. 4.—Log-log composite plot of bridge radius as a function of separation from the hot spot for all 30 bridges with relative normalizations between bridges removed. The best-fit straight line is overlaid and has a slope of  $0.442 \pm 0.005$  with a reduced  $\chi^2$  of 6.8.

## 6.2. Surface Brightnesses as a Function of Lateral Expansion

When the spectral indices,  $\alpha$ , lie in the range 0.6–0.9, which are typical values for these sources, equation (9) predicts a power-law relation between surface brightness and lateral expansion with a power in the range  $-4.7$  to  $-3.9$ . Figure 5 is a log-log composite plot of relative surface brightness,  $S_v/S_{v,0}$ , versus relative bridge width,  $a/a_0$ , for all 30 bridges. The best straight line fit has a slope of  $-4.3 \pm 0.1$  and an intercept of  $0.38 \pm 0.02$  with a reduced  $\chi^2$  of 53. There is a wide range in the uncertainties of the data. A few scattered points with small error bars are responsible for most of the reduced  $\chi^2$ . As a check on the previous fit, a fit with uniform error bars gives a slope of  $-5.1 \pm 0.5$  and an intercept of  $0.36 \pm 0.13$  with a reduced  $\chi^2$  of 1. Finally, a fit fixed to have zero intercept gives a slope of  $-4.0 \pm 0.1$  with a reduced  $\chi^2$  of 1.1. This last fit is the one overlaid on the figure. The slopes of all of these fits are consistent with the prediction of adiabatic expansion (eq. [9]) with  $\alpha$  in the range 0.6–0.9, given that the initial half-width and surface brightness behind the radio hot spot are time-independent for a given source [denoted  $a(x_0)$  and  $S(x_0, 0)$  in eq. (12)]. While individual sources only approximate the behavior of equation (9), the composite plot suggests that cylindrically symmetric adiabatic expansion is the dominant mechanism controlling the change in the low-frequency surface brightness across the bridges of these sources.

## 6.3. Comparison of Predicted and Observed Surface Brightnesses

The surface brightnesses in individual sources can be compared with that predicted by adiabatic expansion in order to see the manner in which individual sources deviate from equation (9). An initial surface brightness,  $S(x_0, 0)$ , is used to predict subsequent surface brightness;

$$S_{\text{predict}}(x, 0) = S(x_0, 0) \left[ \frac{a(x)}{a(x_0)} \right]^{-8\alpha/3 - 7/3}. \quad (12)$$

The starting location,  $x_0$ , is chosen to be a point one or two contours behind the hot spot, and  $S(x_0, 0)$  is taken to be the surface brightness at this location. Of course, any position  $x_0$  could have been used to estimate  $S(x_0, 0)$ . A location just behind the hot spot was chosen to avoid dominance by the

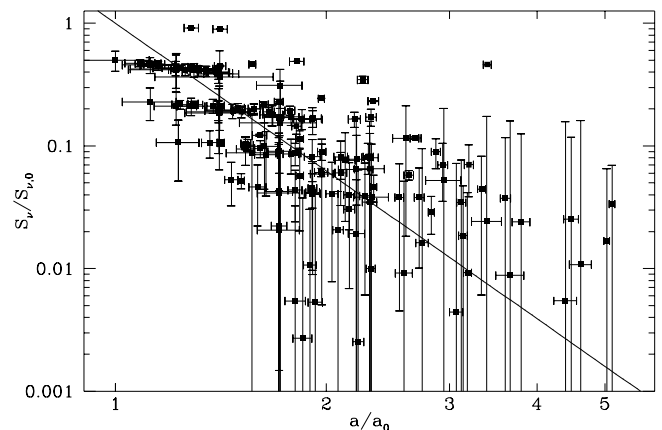


FIG. 5.—Log-log composite plot of surface brightness decrease as a function of bridge width increase for all 30 bridges. The line overlaid has a slope of  $-4.0$  (see § 6.2 for details).

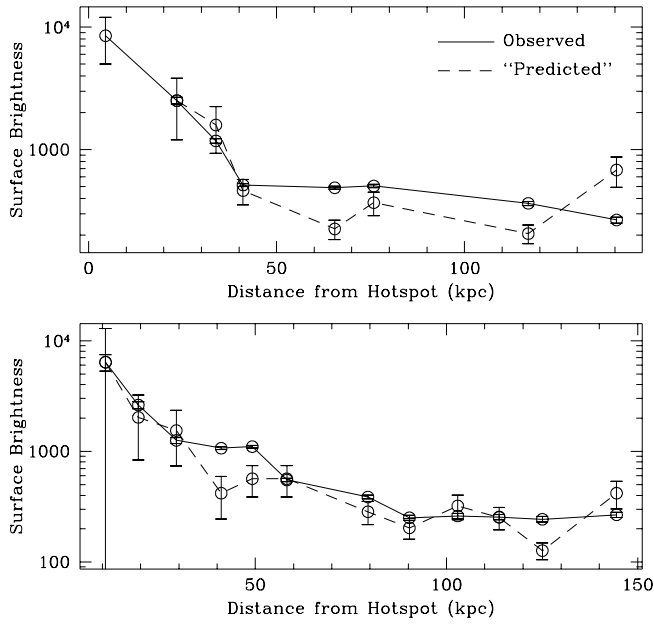


FIG. 6.—The observed and predicted surface brightnesses for 3C 55; the north lobe, as defined in LMS89, is shown in the upper panel; the south lobe, as defined in LMS89, is shown in the lower panel.

hot spot while testing the model over as much of the bridge length as possible. In the absence of precise knowledge of the spectral index at the observing frequency across the sources, a constant value of  $\alpha = 0.7$  is assumed, which, as noted above, is a typical low-frequency value for these sources.

Figures 6, 7, 8, and 9 compare the observed surface brightness (*solid line*) with the predicted surface brightness (*dashed line*) for four of the longer sources: 3C 356 and 3C 55 are the longest sources in the sample, while 3C 268.1 and 3C 267 are the seventh and eighth ranking in length, respec-

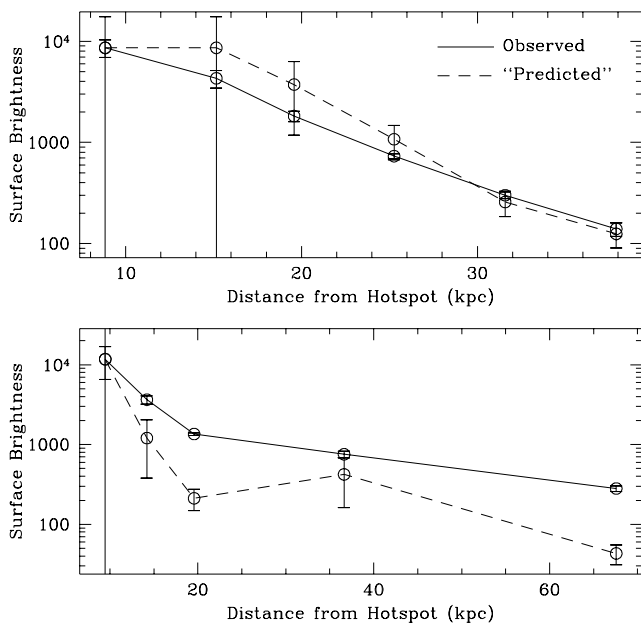


FIG. 7.—The observed and predicted surface brightnesses for 3C 267; the north lobe, as defined in LMS89, is shown in the upper panel; the south lobe, as defined in LMS89, is shown in the lower panel.

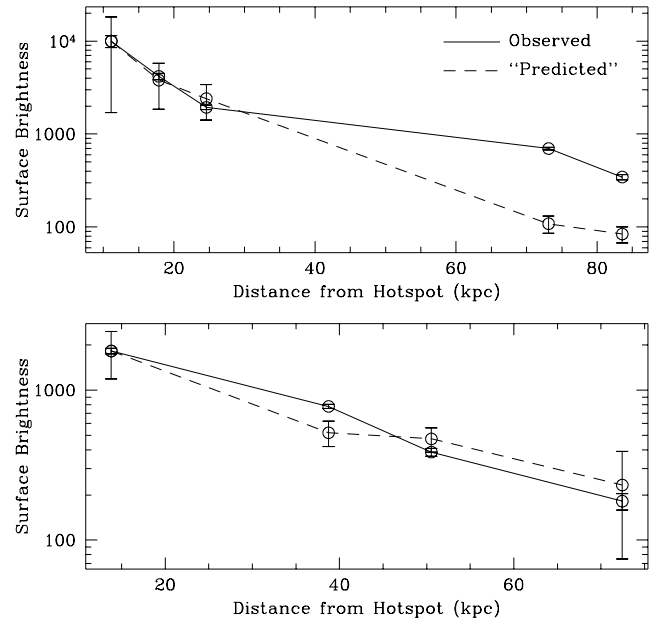


FIG. 8.—The observed and predicted surface brightnesses for 3C 268.1; the north lobe, as defined in LMS89, is shown in the upper panel; the south lobe, as defined in LMS89, is shown in the lower panel.

tively. Note that the normalization of the predicted curve is set so as to match the first point of the observed curve; this normalization is arbitrary, and one is free to alter the vertical normalization of the predicted curve. In general, the predicted and observed curves match quite well, although some deviations are seen. Of the bridges not shown, some match as well or better than those shown; others match more poorly. There does not seem to be a clear pattern to the deviations—indeed, Figure 5 suggests that the deviations are random. Any form of large-scale energy transport or reacceleration in the cocoon would destroy the relation

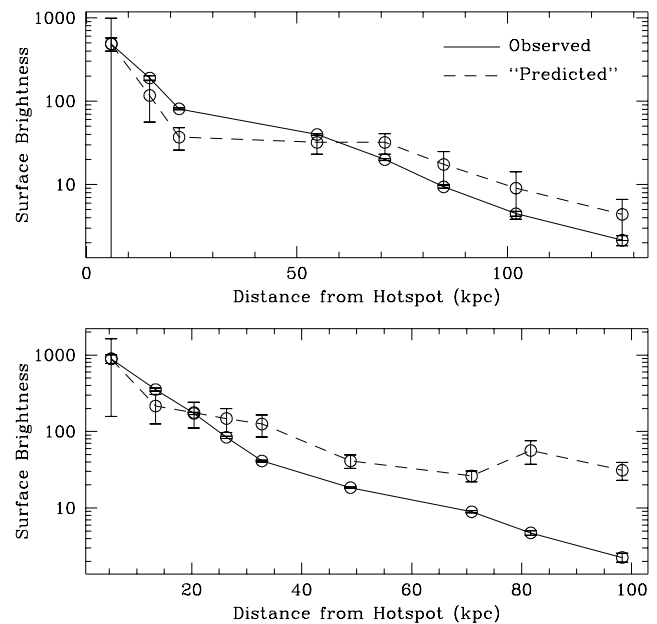


FIG. 9.—The observed and predicted surface brightnesses for 3C 356; the north lobe, as defined in LMS89, is shown in the upper panel; the south lobe, as defined in LMS89, is shown in the lower panel.

in equation (12). The fact that the comparisons are so close suggests that such processes do not dominate the behavior of the bridges.

### 7. THEORY

In § 6.1, it was shown that the bridge width  $a$  as a function of distance from the hot spot  $x$  roughly follows  $a \propto x^{1/2}$ . This behavior was predicted by Begelman & Cioffi (1989) and by Daly (1990), who assume the standard model for the growth of powerful extended radio sources as described, for example, by Begelman et al. (1984). Simple analytic relations may be derived by considering separately the driven shock wave that causes the bridge to become longer at a rate referred to as the lobe propagation velocity  $v_L$ , and the blast wave that causes the bridge to expand in the lateral direction with a velocity  $v_{bw}$  (see, for example, Daly 1990). The blast-wave velocity in the lateral direction falls off with time  $t$  as  $t^{-1/2}$  and terminates when the blast-wave velocity becomes a value of the order of the sound speed of the ambient gas. As shown in §§ III and IVc of Daly (1990), this implies that the bridge width scales as  $a/a_i \propto (t/t_i)^{1/2}$  when the lateral expansion is driven by the blast wave (note that  $v_L$  is denoted  $v_s$ ,  $a$  is denoted  $S$ , and  $x$  is related to  $z$  as defined by Daly 1990; see Fig. 1 in that paper).

It can also be shown that

$$a = a_i \sqrt{x/x_i} \quad (13)$$

when the lobe propagation velocity is constant, which follows since  $x = v_L t$  and  $x_i = v_L t_i$ . The lobe propagation velocity is expected to be constant when the beam power of a given source is time-independent and the mass per unit radius (eq. [2] in Daly 1990) swept up by the forward shock front, at the lobe-medium interface at the head of the bridge, is time-independent; current data are consistent with a lobe propagation velocity that is time-independent for any given source. When the expansion velocity in the lateral direction becomes a value of the order of the sound speed  $c_s$ , the blast wave terminates, and  $a(x)$  is expected to become relatively flat (see Daly 1990 for details). Thus, a break is expected in the behavior of  $a(x)$  at the distance  $x_b$  from the hot spot at which the blast wave terminates. At this point,  $a(x_b) \equiv a_b = a_i(x_b/x_i)^{1/2}$ . Thus, this simple model predicts that at  $x < x_b$ ,  $a = k_L x^{1/2}$ , and for  $x \geq x_b$ ,  $a = \text{constant} = a_b = k_L x_b^{1/2}$ , where  $k_L = a_b/(x_b)^{1/2} = a_i/(x_i)^{1/2}$  (see eq. [15]) assuming that  $a_i$  is constant for a given source.

The two key assumptions adopted here, that  $v_L$  and  $a_i$  are roughly time-independent for a given source, are supported by observations of radio surface brightness as a function of bridge position described in § 6.2. The simplest interpretation of the surface brightness and bridge width as a function of position along the bridge is that the lobe radio power and lobe width (measured just behind the forward shock front at any given time) are roughly time-independent for a given source, and that the expansion in the lateral direction is adiabatic. In this case, it is reasonable to assume that the lobe propagation velocity will also be time-independent, which is consistent with the two assumptions adopted here: that  $v_L$  and  $a_i$  for a given source are time-independent. The fact that the lateral expansion appears to be adiabatic reflects the fact that it is unlikely that radiative losses are important in the radio bridge at the radio frequencies used to study the bridge structure, and that reacceleration of electrons to relativistic energies and backflow are probably negligible within the bridges of these very powerful radio

sources. As noted in § 4, measurements were generally made from low-frequency maps (151 MHz or 1.5 GHz) to reduce the effect of radiative losses.

The lateral expansion velocity at the break is simply related to the Mach number with which the forward shock front propagates into the ambient medium and to the lobe propagation velocity  $v_L$ . The Mach number of lobe advance is  $M = v_L/c_s$ . The expansion velocity in the lateral direction is  $v_{bw} = da/dt = (da/dx)(dx/dt)$  for  $x \leq x_b$ . The sound speed can be approximated by the blast-wave velocity at the break:  $c_s \simeq da/dt|_{x=x_b}$ . For a constant lobe propagation velocity,  $v_L = dx/dt = dx/dt|_{x=x_b}$ , so the Mach number is given by  $M = (da/dx)_{x=x_b}^{-1}$  (see eq. [16]). Thus, the Mach number with which the bridge lengthens can be estimated purely from the geometrical shape of the radio bridge.

Given an independent estimate of the lobe propagation velocity, the temperature of the ambient gas can be estimated. This follows since  $c_s = k_s T^{1/2}$ , so

$$T = \left( \frac{v_L}{k_s M} \right)^2 \quad (14)$$

(see § 8.2 for the value of  $k_s$ ). This equation is used in § 8.2 to estimate the temperature of the ambient gas, assuming that the velocity estimated via the synchrotron and inverse Compton aging model provides a good rough estimate of the lobe propagation velocity.

## 8. APPLICATION TO THE DATA

### 8.1. Mach Number of the Lobe Propagation Velocity

Examining the raw data in Figures 3 and 4 on a source-by-source basis, about half of the sources exhibit a departure or break from the  $a = k_L x^{1/2}$  expansion law at some value of  $x$ . We define such a break to exist if a fit with lower reduced  $\chi^2$  can be found to the form

$$a = \begin{cases} k_L x^{1/2} & x < x_b, \\ k_L x_b^{1/2} \equiv a_b & x \geq x_b, \end{cases} \quad (15)$$

where  $x_b$  is a fit parameter and denotes the location of the break in the power-law expansion profile. Additionally, it is required that at least two data points fall on each side of  $x_b$ . With these criteria, 16 lobes/bridges of the 30 studied here are found to have breaks. Note that for the bridges in which a break is found, the value of  $k_L$  found for that bridge when fitting to equation (15) is different (larger) than that found in § 6.1, fitting the whole bridge to  $a = k_L x^{1/2}$ , and that used to normalize the  $y$ -axis in Figure 4. From this point on, the value of  $k_L$  used for the sources with breaks is that from equation (15).

Figure 10 is a log-log composite plot of normalized bridge half-width,  $a/a_b$ , as a function of normalized separation from the hot spot,  $x/x_b$ , for those 16 bridges, where the break half-width  $a_b$  is  $a_b \equiv [k_L(x_b)^{1/2}]$ . The best-fit straight lines to the  $x < x_b$  and  $x \geq x_b$  regions are overlaid, and have slopes of  $0.49 \pm 0.02$  with a reduced  $\chi^2$  of 1.9 and  $0.04 \pm 0.02$  with a reduced  $\chi^2$  of 2.4, respectively. The reduced  $\chi^2$  include the loss of degrees of freedom from using the parameters  $k_L$  and  $x_b$ .

Equation (10) is derived for a blast wave. When the speed of the wave drops to roughly the sound speed of the external medium, equation (10) will no longer hold. Interpreting the break as signaling the point at which the rate of lateral expansion has fallen to a value of the order of the sound

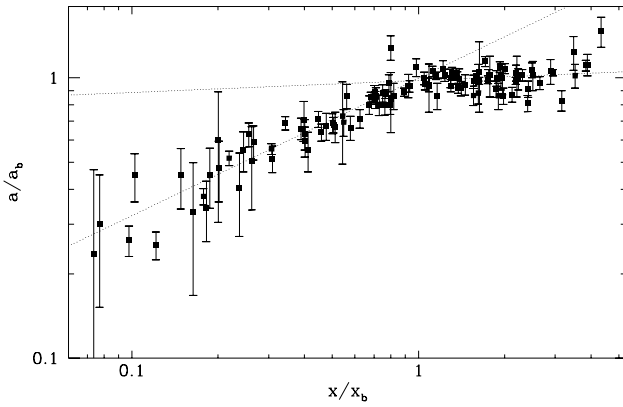


FIG. 10.—Log-log composite plot of normalized bridge radius,  $a/a_b$ , where  $a_b = k_L(x_b)^{1/2}$ , as a function of normalized separation from the hot spot,  $x/x_b$ , for the 16 bridges showing breaks. The best-fit straight lines to the  $x < x_b$  and  $x \geq x_b$  regions are overlaid and have slopes of  $0.49 \pm 0.02$  with a reduced  $\chi^2$  of 1.9 and  $0.04 \pm 0.02$  with a reduced  $\chi^2$  of 2.4, respectively.

speed of the surrounding gas allows a purely geometric estimate, independent of  $H_0$  and  $q_0$ , of the Mach number,  $M$ , of lobe advance. The Mach number is the ratio of the lobe advance velocity to the sound velocity:  $M = v_L/c_s$ . The velocity of lateral expansion is  $da/dt$ , so the sound speed is estimated to be  $da/dt$  evaluated at  $x_b$ . The lobe advance velocity  $v_L = dx/dt$  is assumed to be constant, so it can be evaluated at  $x_b$ . Hence, the Mach number is

$$M = \frac{dx}{dt} \bigg|_{x=x_b} \left( \frac{da}{dt} \bigg|_{x=x_b} \right)^{-1} = \left( \frac{da}{dx} \bigg|_{x=x_b} \right)^{-1} = \frac{2x_b^{1/2}}{k_L} = \frac{2a_b}{k_L^2} = \frac{2x_b}{a_b}. \quad (16)$$

For the bridges where a break is not detected, a conservative  $1\sigma$  lower bound on the Mach number can be estimated by inserting the  $1\sigma$  upper bound on  $k_L$  and a  $1\sigma$  lower bound on  $x_b$  into equation (16); the  $1\sigma$  upper bound on  $k_L$  is used even though a value of  $k_L$  is obtained for each lobe of each source. The  $1\sigma$  lower bound on  $x_b$  is estimated to be  $0.7x_{\max}$ , where  $x_{\max}$  is the maximum extent of the data for that bridge. In fits to the data reported below, only the detections are included in the fit. Table 1 lists the fitted values of  $k_L$ ,  $x_b$ , and  $M$  for all sources studied. The Mach numbers range from about 2.5 to 11, with no obvious distinction between galaxies and quasars.

Figure 11 is a log-log plot of the Mach number of the lobe advance versus core-hot spot separation. For the detections, squares represent sources from LMS89, and circles represent sources from LPR92; the filled symbols represent galaxies, and the open symbols represent quasars. For the limits, diamonds represent galaxies, and crosses represent quasars, with no distinction made between sources drawn from LMS89 and LPR92. It is clear that  $M(r)$  is very flat; the best-fit slope is  $0.20 \pm 0.06$  with a reduced  $\chi^2$  of 6.5, and when the large reduced  $\chi^2$  is accounted for, the slope is  $0.20 \pm 0.15$ , which is consistent with zero slope.

Figure 12 is a log-log plot of the Mach number of the lobe advance versus redshift. The best-fitting straight line shows that the Mach number for this sample is independent of redshift (the slope is  $0 \pm 0.2$  with a reduced  $\chi^2$  of 7.2). This result is not changed significantly by excluding Cygnus

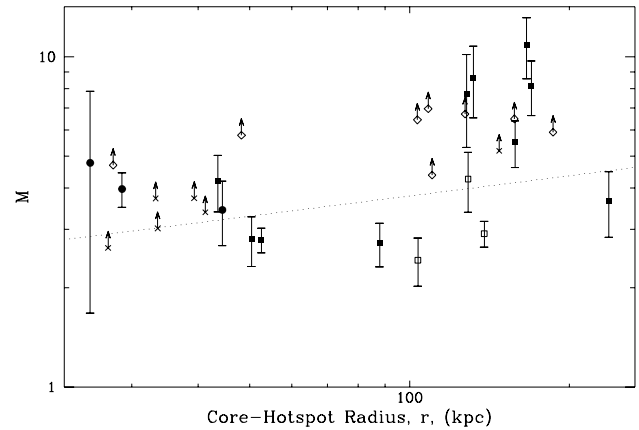


FIG. 11.—Log-log plot of the Mach number of lobe advance vs. core-hot spot separation. For the detections, squares represent sources from LMS89, and circles represent sources from LPR92. Filled symbols represent galaxies, and open symbols represent quasars. For the limits, diamonds are galaxies, and crosses are quasars, with no distinction made between sources drawn from LMS89 and those from LPR92. The best-fit slope is  $0.20 \pm 0.06$  with a reduced  $\chi^2$  of 6.5; bounds are not included in the fit. Scaling the effect of the reduced  $\chi^2$  out of the fit (i.e., scaling the errors to bring the reduced  $\chi^2$  to 1), the slope becomes  $0.20 \pm 0.15$ , which is consistent with zero slope.

A from the fit. A simultaneous fit of Mach number to both core-hot spot separation and redshift,  $M(r, z)$ , gives results indistinguishable from the individual  $M(r)$  and  $M(z)$  fits.

Figure 13 is a log-log plot of the Mach number of the lobe advance versus ambient gas density  $n_a$  at the lobe as determined by WDW97 and Wellman & Daly (1996b). The relation between the Mach number and the ambient gas density is quite flat, with a best-fit slope of  $-0.18 \pm 0.06$  and a reduced  $\chi^2$  of 6.2. Thus, there is little evidence for a correlation between Mach number and ambient gas density, especially when the large  $\chi^2$  of the fit is accounted for, which brings the slope to  $-0.18 \pm 0.15$ .

Core-lobe separation and/or the ambient gas density may have an effect on the lobe shape. Figure 14 is a log-log plot of the shape parameter  $k_L$  versus  $n_a$  at the lobe. The slope of the best fit is  $-0.43 \pm 0.07$  with a reduced  $\chi^2$  of 6.6, indicating that lobes in less dense environments have a larger lobe half-width at a fixed distance behind the hot spot, perhaps because of the faster initial velocity of lateral expansion

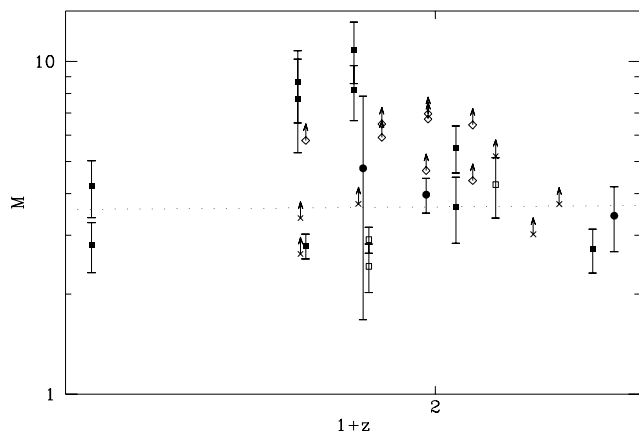


FIG. 12.—Log-log plot of the Mach number of the lobe advance vs. redshift. The symbols are described in the caption to Fig. 11. The best-fit slope is  $0 \pm 0.2$  with a reduced  $\chi^2$  of 7.2; bounds are not included in the fit.

TABLE 1  
SUMMARY OF SOURCE PROPERTIES

Source	Type	$z$	$r^a$	$k_L^b$	$x_b^c$	$M^d$	$T_7^e$	$T_7^f$
LMS89								
3C 55 .....	G	0.720	166	$1.6 \pm 0.2$	$73 \pm 17$	$11 \pm 2$	$3 \pm 2$	$1.5 \pm 0.9$
			170	$1.9 \pm 0.2$	$59 \pm 12$	$8 \pm 2$	$9 \pm 5$	$4 \pm 2$
3C 68.1 .....	Q	1.238	129	$2.7 \pm 0.3$	$34 \pm 8$	$4.3 \pm 0.9$	$21 \pm 11$	$8 \pm 4$
			148	$2.8 \pm 0.1$	$> 55$	$> 5$	$< 47$	$< 16$
3C 175 .....	Q	0.768	104	$3.8 \pm 0.3$	$21 \pm 4$	$2.4 \pm 0.4$	$11 \pm 5$	$6 \pm 3$
			138	$4.3 \pm 0.2$	$39 \pm 5$	$2.9 \pm 0.3$	$9 \pm 3$	$5 \pm 2$
3C 265 .....	G	0.811	158	$2.6 \pm 0.2$	$> 83$	$> 6$	$< 6$	$< 3$
			186	$2.5 \pm 0.2$	$> 65$	$> 6$	$< 4$	$< 2$
3C 267 .....	G	1.144	104	$1.9 \pm 0.2$	$> 47$	$> 6$	$< 6$	$< 3$
			110	$2.1 \pm 0.2$	$> 27$	$> 4$	$< 18$	$< 6$
3C 268.1 .....	G	0.974	108	$2.1 \pm 0.1$	$> 59$	$> 7$	$< 10$	$< 7$
			127	$2.0 \pm 0.1$	$> 51$	$> 7$	$< 5$	$< 3$
3C 322 .....	G	1.681	88	$3.6 \pm 0.3$	$24 \pm 4$	$2.7 \pm 0.4$	$71 \pm 32$	$23 \pm 10$
3C 330 .....	G	0.549	128	$1.6 \pm 0.2$	$36 \pm 13$	$8 \pm 2$	$3 \pm 2$	$2 \pm 1$
			132	$1.6 \pm 0.2$	$50 \pm 14$	$9 \pm 2$	$2 \pm 1$	$2 \pm 1$
3C 356 .....	G	1.079	158	$2.6 \pm 0.2$	$52 \pm 10$	$5.5 \pm 0.9$	$14 \pm 7$	$6 \pm 3$
			237	$3.0 \pm 0.3$	$30 \pm 8$	$3.7 \pm 0.8$	$35 \pm 20$	$14 \pm 8$
3C 405 .....	G	0.056	44	$1.8 \pm 0.2$	$14 \pm 3$	$4.2 \pm 0.8$	$1.0 \pm 0.6$	$0.9 \pm 0.5$
			50	$2.3 \pm 0.2$	$10 \pm 2$	$2.8 \pm 0.5$	$2 \pm 1$	$2 \pm 1$
3C 427.1 .....	G	0.572	48	$1.5 \pm 0.1$	$> 21$	$> 6$	$< 1$	$< 0.6$
			53	$2.7 \pm 0.1$	$14 \pm 1$	$2.8 \pm 0.2$	$2 \pm 1$	$1.4 \pm 0.6$
LPR92								
3C 239 .....	G	1.790	44	$1.9 \pm 0.2$	$11 \pm 3$	$3.4 \pm 0.8$	$79 \pm 50$	$21 \pm 13$
3C 247 .....	G	0.749	25	$1.2 \pm 0.4$	$8 \pm 6$	$5 \pm 3$	$4 \pm 6$	$2 \pm 3$
3C 254 .....	Q	0.734	39	$2.0 \pm 0.1$	$> 15$	$2.8 \pm 0.2$	$< 10$	$< 4$
3C 268.4 .....	Q	1.400	34	$1.5 \pm 0.1$	$> 6$	$> 4$	$< 420$	$< 116$
3C 270.1 .....	Q	1.519	33	$1.6 \pm 0.2$	$> 11$	$> 4$	$< 99$	$< 31$
3C 275.1 .....	Q	0.557	27	$2.3 \pm 0.1$	$> 10$	$> 3$	$< 5$	$< 3$
			41	$1.9 \pm 0.1$	$> 12$	$> 3$	$< 3$	$< 1$
3C 289 .....	G	0.967	28	$1.5 \pm 0.1$	$> 15$	$> 5$	$< 6$	$< 2$
			29	$1.8 \pm 0.1$	$13 \pm 2$	$4.0 \pm 0.5$	$4 \pm 2$	$1.9 \pm 0.8$

<sup>a</sup> Core-hot spot separation in  $h^{-1}$  kpc.

<sup>b</sup> Width fit parameter in  $h^{-1/2}$  kpc $^{1/2}$ .

<sup>c</sup> Hot spot-break distance in  $h^{-1}$  kpc.

<sup>d</sup> Mach number of lobe advance.

<sup>e</sup> Temperature derived for ambient medium ( $\times 10^7$ ) K assuming  $b = \frac{1}{4}$ .

<sup>f</sup> Temperature derived for ambient medium ( $\times 10^7$ ) K assuming  $b = \frac{1}{4}$  and an  $\alpha$ - $z$  correction.

relative to the velocity of lobe advance, than do lobes in more dense environments. Figure 15 is a log-log plot of the parameter  $k_L$  versus  $r$ . The slope of the best fit is  $0.23 \pm 0.02$  with a reduced  $\chi^2$  of 16. These relations are probably a

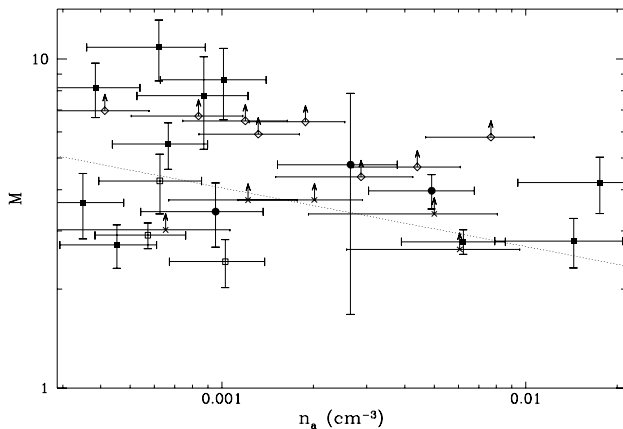


FIG. 13.—Log-log plot of the Mach number of lobe advance vs. ambient gas density. The symbols are described in the caption to Fig. 11. The best-fit slope, including errors in both quantities, is  $-0.18 \pm 0.06$  with a reduced  $\chi^2$  of 6.2. Scaling the reduced  $\chi^2$  to 1, the slope becomes  $-0.18 \pm 0.15$ , which is consistent with zero slope.

result of a combination of  $k_L$  versus  $r$  and the  $n_a$  versus  $r$  relations.

It is not clear whether the fundamental relation is between  $k_L$  and  $r$  or  $k_L$  and  $n_a$  (or  $k_L$  and some other variable). For example, if the outflow direction varies over

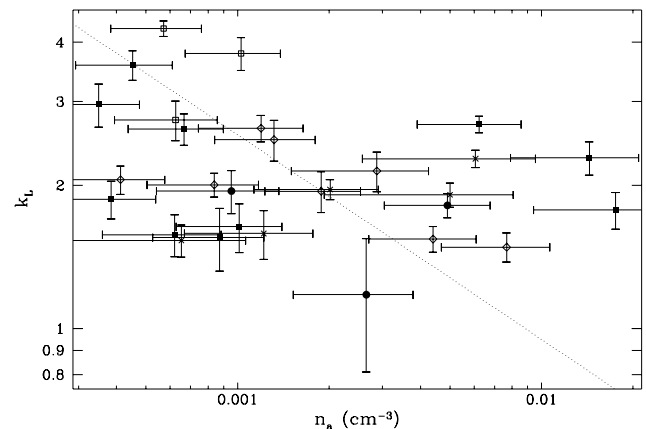


FIG. 14.—Log-log plot of the parameter  $k_L$  vs. ambient gas density. The symbols are described in the caption to Fig. 11. The best-fit slope, including errors in both quantities, is  $-0.43 \pm 0.07$  with a reduced  $\chi^2$  of 6.6. Scaling the reduced  $\chi^2$  to 1, the slope becomes  $-0.43 \pm 0.17$ .

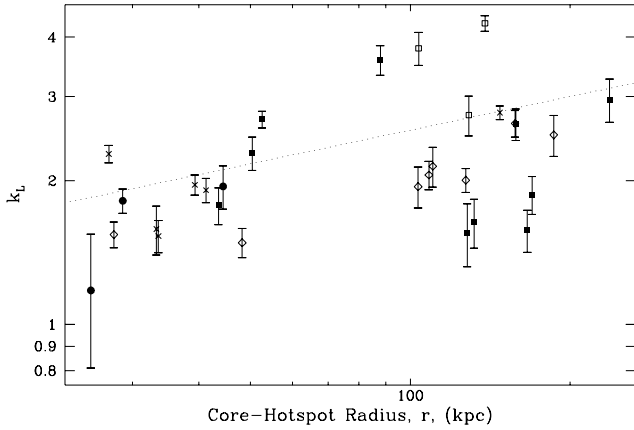


FIG. 15.—Log-log plot of the parameter  $k_L$  vs. core-hot spot separation. The symbols are described in the caption to Fig. 11. The best-fit slope is  $0.23 \pm 0.02$  with a reduced  $\chi^2$  of 16. Scaling the reduced  $\chi^2$  to 1, the slope becomes  $0.23 \pm 0.07$ .

some fixed angle and this sets the initial lobe width, then the initial lobe width will increase as  $r$  increases, which would cause  $k_L$  to increase with  $r$ . In this case, the relation seen between  $k_L$  and  $n_a$  results from the fact that  $n_a$  and  $r$  are related (see WDW97).

### 8.2. Temperature of the Ambient Medium

The Mach number estimate can be combined with an estimate of the lobe advance velocity,  $v_L$ , in order to estimate the temperature of the ambient medium. The velocity is estimated using a synchrotron and inverse Compton aging model (see Pacholczyk 1970, Jaffe & Perola 1973, Myers & Spangler 1985, Alexander & Leahy 1987, Alexander 1987, LMS89, Carilli et al. 1991, and LPR92 for discussions and examples). The velocities used here are derived in WDW97. As in WDW97, the effect of different ratios of the true magnetic field to the minimum-energy magnetic field are considered, as are possible corrections due to the redshift-radio spectral index correlation.

The velocity of sound in a plasma,  $c_s$ , is (e.g., Allen 1973)

$$c_s = \left( \frac{\gamma k T}{m} \right)^{1/2} \left( \frac{n_i + n_e}{n_i} \right)^{1/2}, \quad (17)$$

where  $\gamma = 5/3$  is the adiabatic index for a nonrelativistic plasma,  $k$  is Boltzmann's constant,  $T$  is temperature,  $m$  is the mean molecular mass,  $n_i$  is the number density of ions (nuclei), and  $n_e$  is the number density of electrons. For half-solar abundance, a fully ionized plasma (which is consistent with the observed gas in Cygnus A),  $c_s = (2.8kT/m_p)^{1/2}$ , where  $m_p$  is the mass of a proton. This indicates a temperature

$$T_7 = \left( \frac{c_s}{480 \text{ km s}^{-1}} \right)^2 = \left( \frac{v_L/M}{480 \text{ km s}^{-1}} \right)^2, \quad (18)$$

where  $T_7$  is the temperature in  $10^7$  K. Noting that temperature is a strong function of  $v_L$ , and  $v_L$  is a function of the ratio of the true magnetic field to the minimum-energy magnetic field, we will discuss that ratio before presenting temperatures for this sample.

#### 8.2.1. Departure from Minimum-Energy Conditions

It has been suggested by Carilli et al. (1991) for the case of Cygnus A and Perley & Taylor (1991) for the case of 3C

295 that the true magnetic field strength is about a factor of 3 lower than the minimum-energy value, since this would allow ram pressure confinement of the radio lobe to be consistent with independent X-ray measurements of the ambient gas density. In this section, three different methods are used to estimate the ratio of the true magnetic field strength to the minimum-energy value in Cygnus A. The three methods are ram pressure balance, sound speed/lateral expansion velocity equality at the break, and pressure equilibrium across the bridge-medium interface in the central regions of the source that are distant from the hot spot and longward of the break.

The ram pressure balance equation is  $P \simeq 0.75\rho v_L^2$ . Letting  $B = bB_{\min}$ , both pressure and velocity are functions of  $b$ . The equation for the nonthermal pressure of the relativistic plasma and magnetic field in the radio lobe is

$$P = \left( \frac{4}{3}b^{-3/2} + b^2 \right) B_{\min}^2 / 24\pi, \quad (19)$$

where  $B_{\min}$  is the minimum-energy magnetic field in the lobe. The equation for velocity is

$$v_L = \left[ \frac{x^2 \sigma_T^2 (b^2 B_{\min}^2 + B_{\text{MWB}}^2) v_T}{27\pi e m_e c b B_{\min}} \right]^{1/2}, \quad (20)$$

where  $v_T$  is the break frequency at a distance  $x$  from the hot spot, and  $B_{\min}$  is the lobe/bridge average minimum-energy magnetic field,  $B_{\text{MWB}} = 3.18(1+z)^2 \mu\text{G}$  is the magnetic field strength that yields the energy density of the cosmic microwave background (Jaffe & Perola 1973; LMS89; LPR92; WDW97). Hence, the ram pressure balance equation allows a determination of  $b$  if there is an independent measure of  $\rho$ . The appropriate minimum-energy fields to use in these equations are the lobe minimum-energy field for the nonthermal pressure  $P$ , denoted here by  $B_L$ , and a combination of the lobe and bridge magnetic fields for the velocity (discussed in detail by WDW97), denoted here by  $B_B$ . The equation

$$\frac{b^3 + (4/3)b^{-1/2}}{[b^2 + (B_{\text{MWB}}^2/B_B^2)]^2} = \frac{2\rho x^2 \sigma_T^2 B_B^3 v_T}{3e m_e c B_L^2} \quad (21)$$

can be solved to obtain an estimate of  $b$  if an independent estimate of the ambient gas density  $\rho$  is available. For many cases of interest, such as Cygnus A,  $B \gg B_{\text{MWB}}$  and  $b < 1$ , so the ambient gas density is a very strong function of  $b$ :  $\rho \propto b^{-4.5}$ .

For Cygnus A,  $\rho \simeq 1.12n_a m_p$  with  $n_a \simeq 0.016 \pm 0.004 h^{1/2} \text{ cm}^{-3}$  from *ROSAT* observations (Carilli, Perley, & Harris 1994), where  $n_a$  is the ambient gas density. The  $B_{\min}$ ,  $x$ , and  $v_T$  values are taken from WDW97, and the solution to equation (21), averaging over both lobes, is  $b = 0.25 \pm 0.02$ . Carilli et al. (1991) used an earlier, lower value (Arnaud et al. 1984) for the gas density near the lobes of Cygnus A, so it is not surprising that there is a slight difference between their result ( $b = \frac{1}{3}$ ) and ours. Using an even more recent analysis of *ROSAT* observations (Reynolds & Fabian 1996, who derive a slightly lower gas density [ $n_a = 0.013 \pm 0.002 h^{1/2} \text{ cm}^{-3}$ ] than Carilli et al. 1994), the result is  $b = 0.26 \pm 0.02$ . Derived from the ram pressure in Cygnus A,  $b$  is weakly dependent on  $h$ :  $b \propto h^{-0.175}$ .

The second method of estimating  $b$  is viable when an independent estimate of the ambient gas temperature is available. Equation (18) indicates that  $T \propto (v_L/M)^2$ , and this temperature can be equated with that observed at X-ray energies. The Mach number is obtained as outlined in

§ 7, and the velocity is estimated using equation (20), which is where the value of  $b$  enters. For  $B \gg B_{\text{MWB}}$ , the temperature  $T \propto v_L^2 \propto b^3$ , which is a fairly strong dependence. For a half-solar abundance, fully ionized plasma, the equation

$$b^{-1} \left( b^2 + \frac{B_{\text{MWB}}^2}{B_B^2} \right)^2 = \frac{27\pi e m_e c T_7 M^2 (480 \text{ km s}^{-1})^2}{x^2 \sigma_T^2 B_B^3 v_T} \quad (22)$$

is solved for  $b$ .

For the case of Cygnus A, the Mach number,  $M$ , and the location of the break,  $x_b$ , from § 8.1 are used, and the inputs to equation (20) from WDW97 are used, so all that is needed is an independent measure of the temperature. Reynolds & Fabian (1996) present a temperature profile of the gas in the Cygnus A cluster. Knowing the location of the break, the temperature at that point is determined from the profile. For the north lobe of Cyg A, the temperature in units of  $10^7$  K,  $T_7$ , at the break is  $T_7 \simeq 4.7 \pm 1$ , and the Mach number is  $2.8 \pm 0.5$ . The solution is  $b \simeq 0.32 \pm 0.06$ . (There is another solution near  $b \simeq 1.7 \times 10^{-4}$ , but that solution can be ignored because that great a departure from minimum-energy conditions would lead to a ridiculously large total energy value for the radio emitting plasma.) For the south lobe, the post-hot spot bulge may have distorted the break fit, resulting in a high  $x_b$  and high Mach number, and making the south lobe result less reliable than the north lobe result; the temperature is  $T_7 = 3.4 \pm 0.5$ , and the Mach number is  $4.2 \pm 0.8$ . The solution is  $b = 0.38 \pm 0.08$ , which agrees with the estimate of  $b$  using the other bridge and lobe of the same source. Derived from the temperature at the break in Cygnus A,  $b$  depends on  $h$  weakly:  $b \propto h^{-2/7}$ .

The third method simply equates the nonthermal pressure in the innermost region of the bridge, where lateral expansion has very nearly ceased, to the thermal pressure of the surrounding gas estimated using X-ray data. Thus, the ambient gas pressure indicated by X-ray data is set equal to the nonthermal pressure of the bridge  $P$ , where  $P \propto (1.33b^{-1.5} + b^2)$  (see eq. [19]); unlike the second method, this does not allow a distinction between  $b$  greater than 1 and less than 1. Thus, the three methods are complementary. The first two depend on  $v_L$  and thus depend on the value of  $B_{\text{min}}$  relative to  $B_{\text{MWB}}$ . The first and third depend on the nonthermal pressure of the radio emitting plasma. The first method admits only one solution for  $b$ , except when  $B_{\text{MWB}} \gtrsim 2B_{\text{min}}$  and the right side of equation (21) lies in a very particular range, neither of which happens in cases such as Cygnus A and 3C 295. The second method allows two solutions for  $b$  except when  $B_{\text{min}} \gg B_{\text{MWB}}$ , although one solution is easily discounted. The second method is quite interesting because the dependence on  $b$  is strong and is independent of whether  $b$  is greater than 1 or less than 1. The third method admits two solutions, one with  $b > 1$  and one with  $b < 1$ . Comparison with the results of the first two methods allows a solution to the third to be chosen.

For the case of Cygnus A, equation (19) is used for the nonthermal pressure with  $B_{\text{min}}$ , now the minimum-energy magnetic field in the innermost region of the bridge. The thermal pressure is  $(n_i + n_e)kT$ . This leads to

$$b^2 + \frac{4}{3} b^{-3/2} = \frac{24\pi(n_i + n_e)kT}{B_{\text{min}}^2}. \quad (23)$$

Reynolds & Fabian (1996) present a pressure profile of the gas in the Cygnus A cluster. In the innermost region, they

derive  $(n_i + n_e)T \simeq (2.8 \pm 0.5) \times 10^6 h^{1/2} \text{ K cm}^{-3}$ . There are two solutions for  $b$ . Discarding the one near  $b = 4$  as incompatible with the other analyses, the solution is  $b \simeq 0.21 \pm 0.03 h^{-0.38}$ . This solution should be treated as a lower limit because two effects in the inner bridge may cause the pressure to be higher than the minimum-energy magnetic field would indicate. The first is that spectral aging may have reduced the surface brightness even on the 151 MHz map (LMS89) used to calculate  $B_{\text{min}}$ . The other is that in the innermost bridge, the oldest region of the source, it is possible that the bridge material and the surrounding gas may have mixed to some extent. If mixing occurs, the non-thermal pressure in the lobe is equal to some unknown fraction ( $< 1$ ) of the thermal pressure, so  $b$  is larger than the value derived when assuming no mixing. Note that in equation (23), for  $b$  in the range of the solution, the left-hand side behaves as  $b^{-1.5}$ , not as strong a function of  $b$  as for the other two methods of determining  $b$ , but interesting nonetheless.

Taken together, these three determinations of  $b$  argue strongly for a value of  $b$  of about  $\frac{1}{4}$  to  $\frac{1}{3}$  and suggest that the value of  $b$  is constant throughout the radio bridge.

### 8.2.2. Temperature Results

Here the ambient gas temperature is estimated using equation (18), and the velocity data from WDW97 assuming  $b = \frac{1}{4}$ , except where explicitly noted. Figure 16 is a log-log plot of the estimated temperature versus core-hot spot separation. As in Figure 11, LMS89 sources with an estimate of the Mach number, and hence of temperature, are represented by squares, while those from LPR92 are represented by circles; filled symbols represent galaxies, and open symbols represent quasars. For the limits, diamonds represent galaxies, and crosses represent quasars, with no distinction made between sources drawn from LMS89 and LPR92. To obtain temperature bounds for those sources with a bound on the Mach number, i.e., those without a detected break, the  $1\sigma$  lower bound on  $M$  and the  $1\sigma$  upper bound on  $v_L$  are substituted into equation (18).

In fits to the data, only the detections are included in the fit. The best-fit straight line is overlaid on Figure 16 and has a slope of  $0.7 \pm 0.2$  with a reduced  $\chi^2$  of 5.4. This might

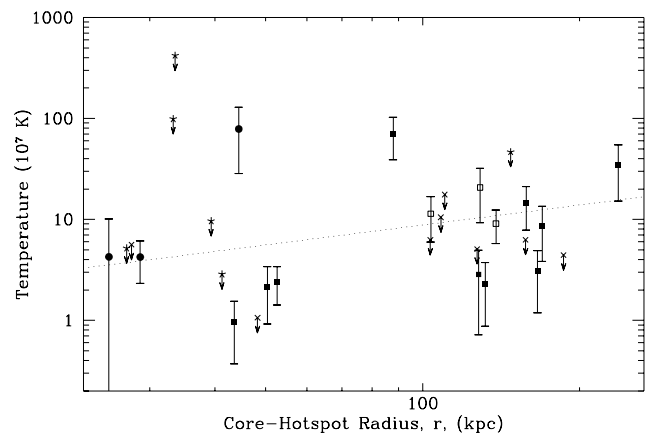


FIG. 16.—Log-log plot of the ambient gas temperature vs. core-hot spot separation. The symbols are described in the caption of Fig. 11. The best-fit slope is  $0.7 \pm 0.2$  with a reduced  $\chi^2$  of 5.4.

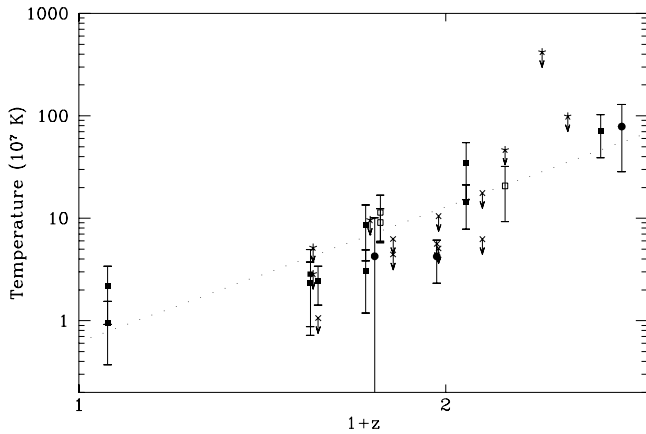


FIG. 17.—Log-log plot of the ambient gas temperature vs. redshift. The symbols are described in the caption of Fig. 11. The best-fit slope is  $4.4 \pm 0.5$  with a reduced  $\chi^2$  of 1.3.

have suggested that some of the smaller sources are in cooling flow regions; however, when the large reduced  $\chi^2$  is considered, the slope becomes  $0.7 \pm 0.5$ , which is consistent with zero slope at about  $1 \sigma$ . It is interesting to note that for sources with two temperature determinations, one from each side of the radio source, the temperature determinations are generally in good agreement.

The fact that the temperature does not vary with core-lobe separation suggests that the sources are in roughly isothermal gaseous environments. The weighted mean of the temperatures is  $(2.1 \pm 0.4) \times 10^7$  K, the unweighted mean is  $(17.5 \pm 6.3) \times 10^7$  K, and the median is  $(5.6 \pm 2.8) \times 10^7$  K.

Figure 17 is a log-log plot of the ambient gas temperature versus redshift. The best-fit straight line has a slope of  $4.4 \pm 0.5$  with a reduced  $\chi^2$  of 1.3. A combined fit,  $T \propto r^f(1+z)^g$ , gives  $f = 0.3 \pm 0.5$ ,  $g = 4.2 \pm 1.5$  with a reduced  $\chi^2$  of 1.2; again, the fact that  $f$  is consistent with zero at  $2 \sigma$  suggests that the sources are in roughly isothermal environments. The error ellipsoid is shown in Figure 18 and indicates that the parameters  $f$  and  $g$  are not strongly correlated. The results of all temperature fits are given in Table 2. The Mach number of the lobe advance is not a

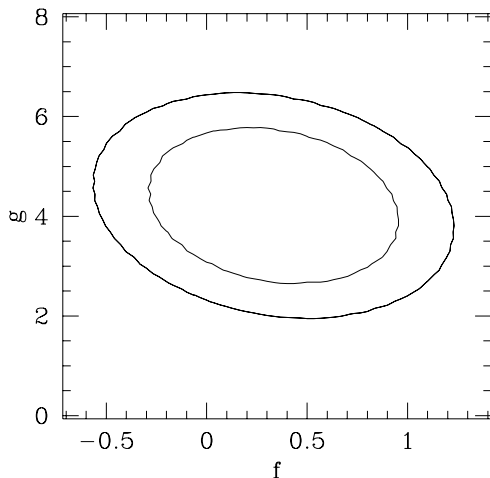


FIG. 18.—Error ellipsoid on the parameters  $f$  and  $g$  in the fit  $T \propto r^f(1+z)^g$  for the temperature data shown in Figs. 16 and 17. The parameters  $f$  and  $g$  are not strongly correlated.

TABLE 2

TEMPERATURE FIT RESULTS FOR  $T \propto r^f(1+z)^g$ 

$b$	$q_0$	$\alpha-z$ ? <sup>a</sup>	$f$	$g$	$r\chi^2$
$\frac{1}{4}$ .....	0	No	$0.7 \pm 0.2$	$\equiv 0$	5.4
$\frac{1}{4}$ .....	0	No	$\equiv 0$	$4.4 \pm 0.5$	1.3
$\frac{1}{4}$ .....	0	No	$0.3 \pm 0.5$	$4.2 \pm 1.5$	1.2
$\frac{1}{4}$ .....	0	Yes	$0.6 \pm 0.2$	$\equiv 0$	3.3
$\frac{1}{4}$ .....	0	Yes	$\equiv 0$	$3.2 \pm 0.5$	1.3
$\frac{1}{4}$ .....	0	Yes	$0.3 \pm 0.6$	$3.0 \pm 1.5$	1.2
$\frac{1}{4}$ .....	0.5	No	$0.6 \pm 0.2$	$\equiv 0$	3.9
$\frac{1}{4}$ .....	0.5	No	$\equiv 0$	$3.5 \pm 0.5$	1.4
$\frac{1}{4}$ .....	0.5	No	$0.4 \pm 0.6$	$3.4 \pm 1.6$	1.3
$\frac{1}{4}$ .....	0.5	Yes	$0.5 \pm 0.2$	$\equiv 0$	2.3
$\frac{1}{4}$ .....	0.5	Yes	$\equiv 0$	$2.3 \pm 0.5$	1.4
$\frac{1}{4}$ .....	0.5	Yes	$0.4 \pm 0.6$	$2.2 \pm 1.7$	1.3
1.....	0	No	$0.2 \pm 0.2$	$\equiv 0$	1.9
1.....	0	No	$\equiv 0$	$2.2 \pm 0.6$	0.9
1.....	0	No	$0 \pm 0.6$	$2.2 \pm 1.6$	0.9

<sup>a</sup> Indicates whether or not the  $\alpha-z$  correction discussed in § 8.2.2 is applied.

strong function of redshift, and most of the strength of the  $T(z)$  relation is a result of the correlation in this sample between  $v_L$  and  $z$ , a correlation whose strength depends on the correlation between spectral index and redshift (and any correction applied to that correlation), which is discussed in WDW97. In WDW97, a correction to the initial spectral index is presented; this correction amounts to shifting the observed spectral index of a source at redshift  $z$  to zero redshift using the slope ( $0.8 \pm 0.2$ ) of the observed  $\alpha-z$  correlation. The observed correlation is  $\alpha = \alpha(z=0) + (0.8 \pm 0.2) \log(1+z)$  (WDW97), where the best-fit line has an intercept of  $\alpha(z=0) = (0.65 \pm 0.05)$ . Figure 19 shows the correlation between  $v_L$  and  $z$  in the uncorrected case (*left panel*) and the corrected case (*right panel*). It is not clear what the correct way to account for the  $\alpha-z$  correlation is. There are other possible correction methods, and their evaluation is ongoing (Wan & Daly 1997). Figure 20 is a log-log plot of temperature versus redshift assuming the spectral index correction given in WDW97. The best straight line fit is overlaid and has a slope of  $3.2 \pm 0.5$  with a reduced  $\chi^2$  of 1.3. The combined fit,  $T \propto r^f(1+z)^g$ , gives  $f = 0.3 \pm 0.6$ ,  $g = 3.0 \pm 1.5$  with a reduced  $\chi^2$  of 1.2. Table 1 lists the temperatures derived both with and without the  $\alpha-z$  correction for  $b = \frac{1}{4}$ .

While § 8.2.1 argues strongly for a value of  $b$  of about  $\frac{1}{3}$  to  $\frac{1}{4}$ , if some alternative method could be found to balance the

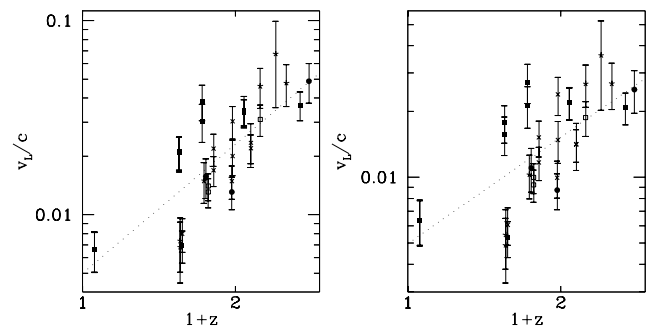


FIG. 19.—Log-log plots of the lobe velocities  $v_L$  vs. redshift without any correction (*left panel*) and assuming the correction to spectral indices discussed in § 8.2.2 (*right panel*). The best-fit slopes are  $2.2 \pm 0.2$  with a reduced  $\chi^2$  of 3.6 (*left panel*) and  $1.6 \pm 0.2$  with a reduced  $\chi^2$  of 3.8 (*right panel*).

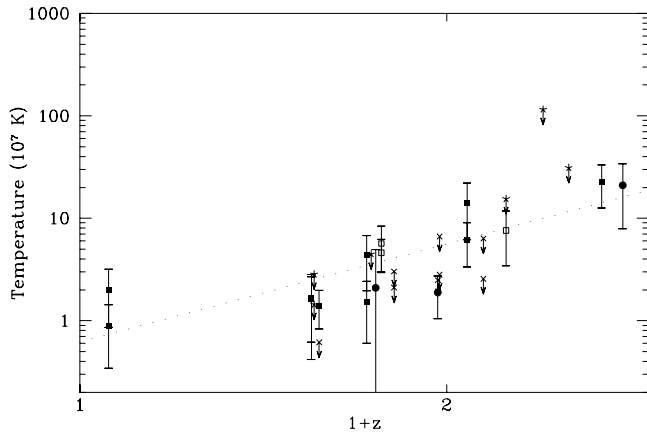


FIG. 20.—Log-log plot of the ambient gas temperature vs. redshift assuming the correction to radio spectral indices discussed in § 8.2.2. The best-fit slope is  $3.2 \pm 0.5$  with a reduced  $\chi^2$  of 1.3.

ambient gas pressure, ram pressure, and temperature equations, a weaker  $T(z)$  relation would be found. For  $b = 1$ , the fit  $T \propto (1+z)^g$  gives  $g = 2.2 \pm 0.6$  with a reduced  $\chi^2$  of 0.9. The combined fit,  $T \propto r^f(1+z)^g$ , gives  $f = 0.0 \pm 0.6$ ,  $g = 2.2 \pm 1.6$  with a reduced  $\chi^2$  of 0.9. Figure 21 shows the temperatures derived assuming  $b = 1$ , normalized to match the observed temperature in Cygnus A. Without normalization to Cygnus A, the temperatures would be a factor of 25 higher.

The temperature (assuming  $b = \frac{1}{4}$  and no  $\alpha$ - $z$  correction) is plotted as a function of radio power at 178 MHz in Figure 22 for two redshift bins,  $z < 1$  (left panel) and  $z > 1$  (right panel), in an attempt to understand whether or not a power-temperature correlation combined with the radio power-redshift selection effect could explain the  $T(z)$  relation. This suggests that the  $z < 1$  subsample is not dominated by selection effects associated with working with a flux-limited sample, since temperature and power are not correlated, while that at  $z > 1$  is. However, when the temperature as a function of redshift is computed for each redshift range separately (see Fig. 23), a significant increase of temperature with redshift is seen in both redshift subsamples separately. This could be because the number of points is very small, and the bounds are not included in the

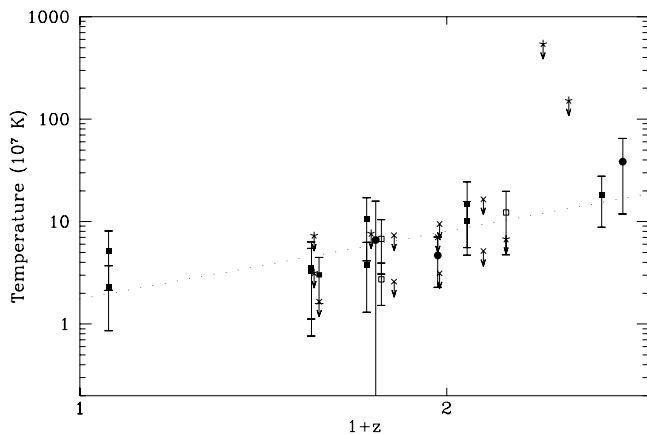


FIG. 21.—Log-log plot of the ambient gas temperature vs. redshift assuming  $b = 1$ , normalized to match the observed temperature in Cygnus A. Without normalization, the temperatures would be a factor of 25 higher. The best-fit slope is  $2.2 \pm 0.5$  with a reduced  $\chi^2$  of 0.9.

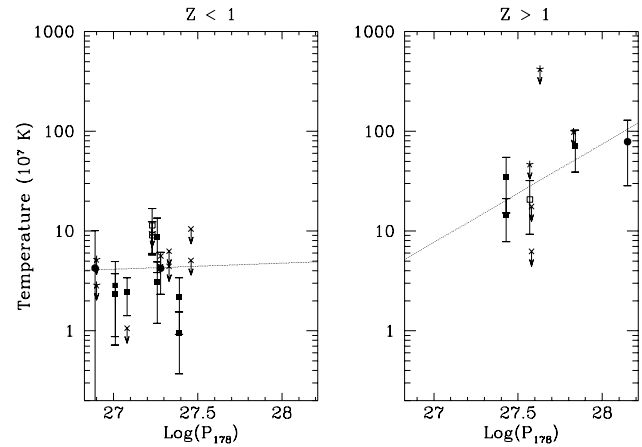


FIG. 22.—Log-log plot of ambient gas temperature, assuming  $b = \frac{1}{4}$  and no  $\alpha$ - $z$  correction, vs. radio power with the data divided into two redshift bins,  $z < 1$  (left panel) and  $z > 1$  (right panel). The best-fit slopes are  $0.0 \pm 0.6$  with a reduced  $\chi^2$  of 2.3 and  $1.0 \pm 0.4$  with a reduced  $\chi^2$  of 0.8, respectively.

fit; it might also be affected by the sources for which we have two temperature estimates that are both included in the fit as independent measurements, or by the quasar in the low-redshift bin that has a large temperature estimate that might be affected by projection effects; all of these possibilities are considered and discussed in more detail by Wan & Daly (1997). It is interesting to note that when the  $\alpha$ -corrected velocities are used,  $T(z)$  for the  $z < 1$  subsample is consistent with zero slope, while  $T(z)$  for the  $z > 1$  subsample is increasing, which may indicate that the flux-limited selection effect is affecting the higher redshift sources more strongly than the low-redshift sources. This causes a general worry about the accuracy of velocities estimated using synchrotron and inverse Compton aging, as discussed in § 10.

### 8.3. Cooling Time

The ambient gas temperature may be combined with the ambient gas density to estimate the cooling time of the gas.

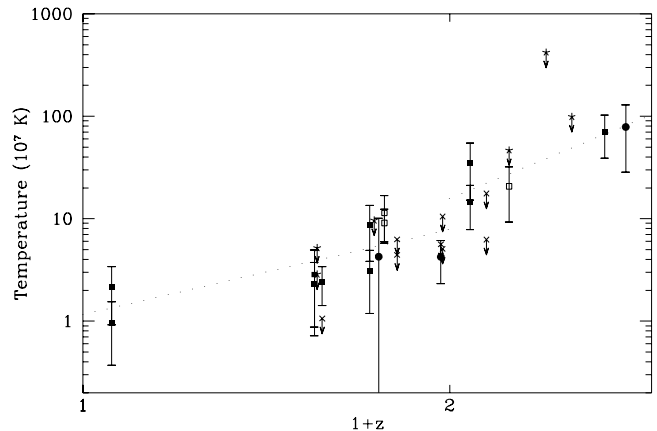


FIG. 23.—Log-log plot of the ambient gas temperature vs. redshift with  $b = \frac{1}{4}$  and no  $\alpha$ - $z$  correction (i.e., the same as Fig. 17) and with the data divided into two redshift bins,  $z < 1$  and  $z > 1$ . The best-fit slopes are  $2.8 \pm 0.9$  with a reduced  $\chi^2$  of 1.2 and  $4.9 \pm 1.9$  with a reduced  $\chi^2$  of 0.6, respectively.

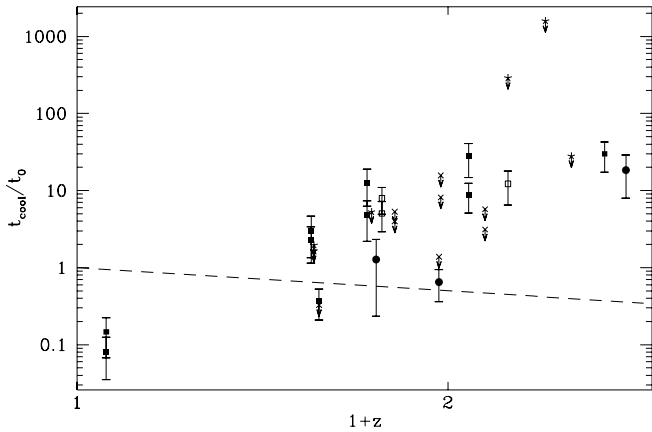


FIG. 24.—Log-log plot of the ratio of cooling time to the current age of the universe, derived for the ambient medium at the position of the radio lobes, vs. redshift, assuming  $b = \frac{1}{4}$  and no  $\alpha$ - $z$  correction. The dashed line is  $t/t_0$ , the ratio of the age of the universe to the current age of the universe. Points below the line represent “cooling flow” regions, while points above the line represent regions that are not cooling on astrophysically interesting timescales.

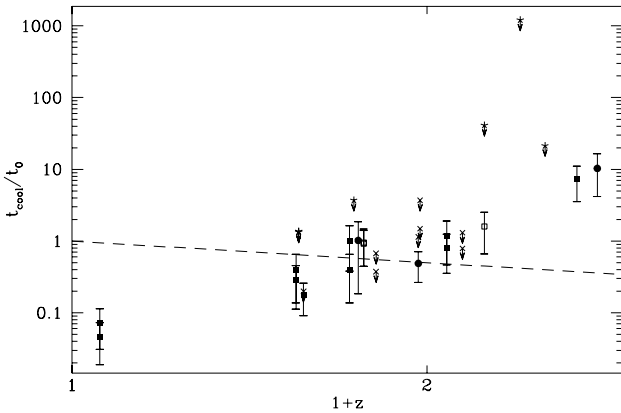


FIG. 25.—Log-log plot of the ratio of estimated *central* cooling time of the ambient gas to the current age of the universe vs. redshift, assuming  $b = \frac{1}{4}$  and no  $\alpha$ - $z$  correction. Points below the line represent cooling flow regions, while points above the line represent regions that are not cooling on astrophysically interesting timescales.

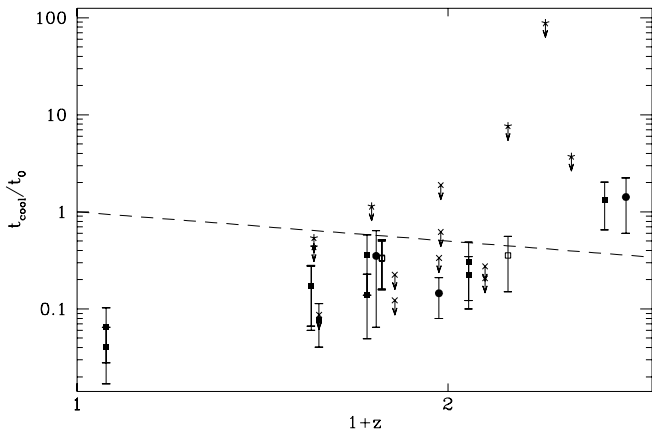


FIG. 26.—Log-log plot of the ratio of estimated *central* cooling time to the current age of the universe, derived for the ambient medium, vs. redshift, assuming  $b = \frac{1}{4}$  and the correction to radio spectral indices discussed in § 8.2.2. Points below the line represent cooling flow regions, while points above the line represent regions that are not cooling on astrophysically interesting timescales.

The energy density,  $u$ , of the ambient gas is

$$u = \frac{3}{2}(n_i + n_e)kT, \quad (24)$$

where  $n_i$  is the number density of ions (nuclei),  $n_e$  is the number density of electrons,  $k$  is Boltzmann’s constant, and  $T$  is temperature. Considering cooling only by thermal bremsstrahlung, which dominates other mechanisms at these temperatures, the bolometric emissivity is (e.g., Rybicki & Lightman 1979)

$$\varepsilon = \left(\frac{2\pi kT}{3m}\right)^{1/2} \frac{32\pi e^6}{3hmc^3} n_i n_e Z^2 \bar{g}_B, \quad (25)$$

where  $m$  is the electron mass,  $e$  is the electron charge,  $h$  is Planck’s constant,  $\bar{g}_B \simeq 1.2$  is the frequency average of the velocity-averaged Gaunt factor, and  $Z \simeq 1.1$  is the average charge on the nuclei in the Hydrogen-Helium plasma,  $n_i Z = n_e$ . Hence, the cooling time,  $t_{\text{cool}}$ , in units of  $10^9$  yr is

$$t_{\text{cool}} = \frac{u}{\varepsilon} \simeq 2.1 \times 10^{-2} \frac{T_7^{1/2}}{n_e} \text{ Gyr}, \quad (26)$$

where  $n_e$  is given in units of  $\text{cm}^{-3}$ , and  $T_7$  is the temperature in units of  $10^7$  K.

Combining the ambient temperature estimates of § 8.2.2 with ambient gas density estimates from WDW97 gives an estimate of  $t_{\text{cool}}$  at the position of the lobe. Figure 24 is a plot of the ratio of  $t_{\text{cool}}$  at the lobe to  $t_0$ , the current age of the universe, versus redshift. The current age of the universe has been taken to be 14 Gyr. The dashed line indicates a cooling time equal to the age of the universe at that redshift. Sources above the line are in environments that are not cooling at the radius of the lobes; sources below the line likely are. Only two sources are almost certainly to be in environments that are cooling at the radius of the lobes.

A more interesting question is how many of the sources are located in environments that are cooling in the central, most dense regions. In the absence of direct estimates for the central densities, the core number density is estimated by scaling the density estimate near the lobe to the center by assuming a King model and using the model parameters obtained by WDW97. The parameters used here are  $r_{\text{core}} = 50 h^{-1}$  kpc and  $\beta = 0.7$ . Figure 25 is a plot of the ratio of  $t_{\text{cool}}$  at the core to  $t_0$ , the current age of the universe, versus redshift. The line indicates a cooling time equal to the age of the universe at that redshift. Sources above the line have cooling times greater than the age of the universe at the redshift of the source, and sources below the line have cooling times less than the age of the universe at that redshift, and hence they are “cooling flow regions.” Many sources may be in environments that are cooling at their centers.

Recalling the possibility of a correction to spectral indices discussed in § 8.2.2, Figure 26 is a plot of the ratio of  $t_{\text{cool}}$  at the core to  $t_0$ , the current age of the universe, versus redshift assuming that correction. In this case, almost all the sources are in environments in which cooling is important at their centers.

## 9. EFFECTS OF ASSUMED COSMOLOGY

As noted in the § 1, all the results described above assume  $q_0 = 0$ . Considering the case  $q_0 = 0.5$  leads to almost no changes other than lowering the implied temperatures and cooling times at high redshift. In particular, Figure 5, the ratio of surface brightnesses as a function of the ratio of

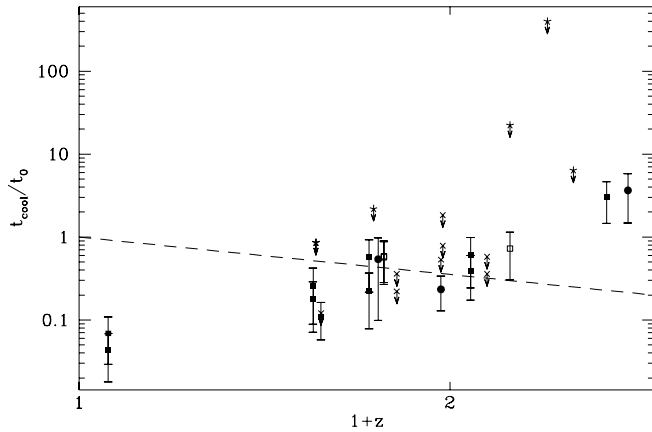


FIG. 27.—Log-log plot of the ratio of estimated *central* cooling time to the current age of the universe, derived for the ambient medium, vs. redshift, assuming  $b = \frac{1}{4}$ ,  $q_0 = 0.5$ , and no  $\alpha$ - $z$  correction. Points below the line represent cooling flow regions, while points above the line represent regions that are not cooling.

bridge widths, and Figure 10, the normalized bridge half-width as a function of the normalized distance from the hot spot, are completely independent of  $q_0$ , as are the Mach number estimates.

Figure 27 is a plot of the ratio of  $t_{\text{cool}}$  at the core to  $t_0$ , the current age of the universe, versus redshift assuming  $q_0 = 0.5$ . The analogous plot for  $q_0 = 0$  is Figure 25. The spatially flat cosmology has little effect on the number of sources that are likely to be in cooling environments; some of the borderline cases are slightly more likely to be cooling if  $q_0 = 0.5$  than if  $q_0 = 0$ .

Figure 28 is a plot of the ratio of  $t_{\text{cool}}$  at the core to  $t_0$ , the current age of the universe, versus redshift assuming  $q_0 = 0.5$  and the correction to spectral indices discussed in § 8.2.2. The analogous plot for  $q_0 = 0$  is Figure 26. As in Figure 26, almost all the sources are in environments that are likely to be cooling at their centers.

Figure 29 is a log-log plot of temperature versus redshift assuming  $q_0 = 0.5$ . The best-fit straight line is overlaid and has a slope of  $3.5 \pm 0.5$  with a reduced  $\chi^2$  of 1.4. The analogous plot for  $q_0 = 0$  is Figure 17. The combined fit,  $T \propto r^f(1+z)^g$ , gives  $f = 0.4 \pm 0.6$ ,  $g = 3.4 \pm 1.6$  with a

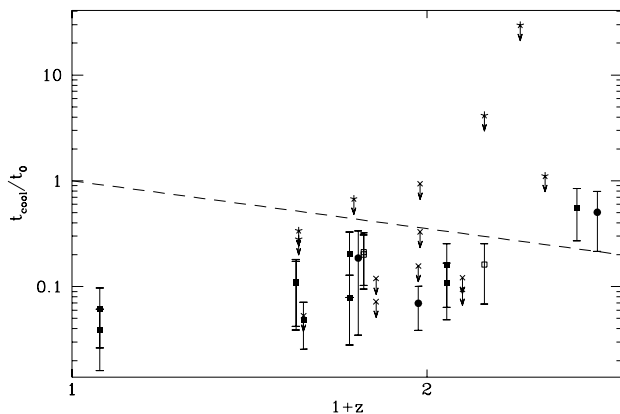


FIG. 28.—Log-log plot of the ratio of estimated *central* cooling time to the current age of the universe, derived for the ambient medium, vs. redshift, assuming  $b = \frac{1}{4}$ ,  $q_0 = 0.5$ , and the correction to radio spectral indices discussed in § 8.2.2. Points below the line represent cooling flow regions, while points above the line represent regions that are not cooling.

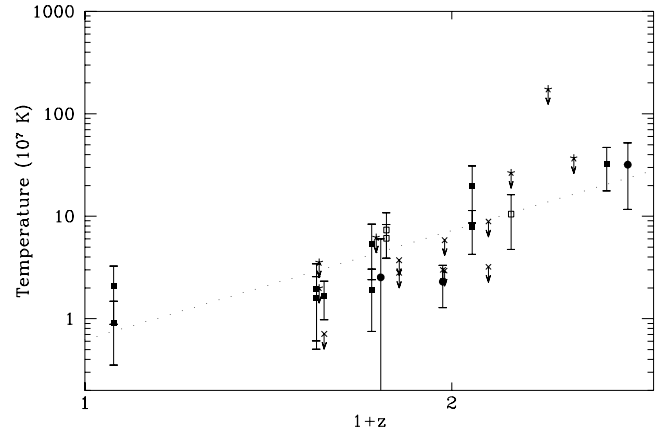


FIG. 29.—Log-log plot of the ambient gas temperature vs. redshift assuming  $b = \frac{1}{4}$ ,  $q_0 = 0.5$ , and no  $\alpha$ - $z$  correction. The best-fit slope is  $3.5 \pm 0.5$  with a reduced  $\chi^2$  of 1.4.

reduced  $\chi^2$  of 1.3. The strength of the  $T(z)$  relation is weaker for  $q_0 = 0.5$  than for  $q_0 = 0$  but is still significant. Selection effects and systematics that may be responsible for the  $T(z)$  relation are discussed in §§ 8.2.2 and 10.

Figure 30 is a log-log plot of temperature versus redshift assuming  $q_0 = 0.5$  and the correction to radio spectral indices. The best straight line fit is overlaid and has a slope of  $2.3 \pm 0.5$  with a reduced  $\chi^2$  of 1.4. The analogous plot for  $q_0 = 0$  is Figure 20. The combined fit,  $T \propto r^f(1+z)^g$ , gives  $f = 0.4 \pm 0.6$ ,  $g = 2.2 \pm 1.7$  with a reduced  $\chi^2$  of 1.3. The strength of the  $T(z)$  relation is weaker for  $q_0 = 0.5$  than for  $q_0 = 0$  and does not exhibit evolution with redshift that is significant statistically.

Cosmologies with a nonzero cosmological constant are not considered here and are left for future work.

## 10. SUMMARY AND CONCLUSIONS

Models of an overpressured cocoon expanding as a blast wave into the external medium are supported. The expansion clearly follows a square root law,  $a \propto x^{1/2}$ , with the half-width of the bridge,  $a$ , increasing with distance,  $x$ , from the hot spot until a break is reached in some sources, as predicted, for example, by Daly (1990).

The surface brightness falloff along individual bridges is well matched by the prediction of adiabatic cooling due to

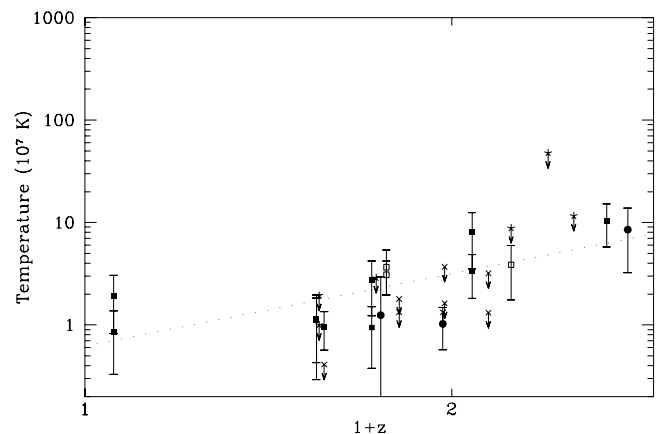


FIG. 30.—Log-log plot of the ambient gas temperature vs. redshift assuming  $b = \frac{1}{4}$ ,  $q_0 = 0.5$ , and the correction to radio spectral indices discussed in § 8.2.2. The best-fit slope is  $2.3 \pm 0.5$  with a reduced  $\chi^2$  of 1.4.

lateral expansion, assuming that the initial lobe radio surface brightness and half-width are time-independent for a given source. This is seen in the sample as a whole and in many individual sources. The bridge surface brightness at position  $x$  is predicted by assuming that the initial value of the surface brightness was the same as the value that is presently close to the lobe and hot spot, and that the bridge expanded by an amount given by the ratio of the bridge width at position  $x$  relative to that just behind the lobe and hot spot. Thus, the remarkably good fit between the model predictions and the data suggest that, for a given radio source, the radio power and lobe radius are indeed roughly time-independent, and that the expansion in the lateral direction is adiabatic. This indicates that there is little reacceleration of relativistic electrons in the radio bridge and that the transport of relativistic plasma by backflows is probably negligible in the very powerful extended radio sources studied here. Thus, significant portions of the bridges of powerful radio sources are “quiescent,” and at low frequencies, adiabatic expansion is likely to be the dominant cooling mechanism. Areas close to the hot spots may show signs of turbulence or backflow and cannot be considered quiescent, as indicated in high-resolution images of the hot spot regions of Cygnus A (Perley & Carilli 1996; Carilli et al. 1996).

The issue of whether or not backflow is important in powerful extended radio sources has been addressed recently by Scheuer (1995, 1996), who examined the lobe-length asymmetry of a sample of powerful radio sources and reported that growth speeds of lobes are typically a few percent of the speed of light. This is consistent with the lobe propagation speeds estimated for this sample (WDW97), and for the sample discussed by Daly (1995). The weighted mean lobe propagation velocity and standard deviation of the mean for the sample described in this paper is  $(0.045 \pm 0.002)c$  for  $b = 1$ , or  $(0.011 \pm 0.0004)c$  for  $b = \frac{1}{4}$ ; the average value for the sample discussed by Daly (1995), who assumed  $b = 1$ , is  $(0.04 \pm 0.005)c$ , where  $c$  is the speed of light.

Scheuer (1995) notes that growth speeds derived from spectral aging for some sources in LPR92 are much larger than those derived from source asymmetry and concludes that backflow is important in such sources. However, as shown above, the lobe propagation velocities for sources in this sample and the sample considered by Daly (1995) are completely consistent with those derived from source asymmetry. Thus, it is unlikely that backflow is significant for the current sample. This is also consistent with implications based on observations of the bridge shape and structure of powerful radio sources (Alexander & Leahy 1987; Carilli et al. 1991). Furthermore, combining the Mach number of lobe advance with the lobe propagation velocity estimated using the synchrotron and inverse Compton aging model for Cygnus A yields a prediction of the ambient gas temperature that matches the temperature indicated by X-ray measurements (assuming  $b = 0.25$  as derived in two other independent regions of the source; see § 8.2.1 for details), which also suggests that the velocity estimated using a standard aging model that assumes negligible backflow provides a good rough estimate of the true lobe propagation velocity.

For those sources in which a break in the square root expansion law,  $a \propto x^{1/2}$ , is seen, a purely geometric estimate of the Mach number of the lobe advance may be obtained,

which is independent of the specific cosmological parameters adopted. Typical Mach numbers obtained range from about 2 to about 10 and appear to be independent of redshift and radio source size (i.e., core-hot spot separation).

The Mach number may be combined with the lobe velocity (estimated from synchrotron and inverse Compton aging) to estimate the temperature of the ambient gas surrounding the radio source. The temperature estimated in this way is strongly correlated with redshift. This may be due to selection effects associated with the radio spectral index-redshift selection effect or the radio power-redshift selection effect. However, it is clear that the temperatures are cluster-like, with typical values ranging from a few to several keV (see § 8.2.2 and Table 1), which suggests that very powerful radio sources are located in cluster-like gaseous environments. Not only are the temperatures cluster-like, but the ambient gas densities are cluster-like as well (WDW97). The temperatures and densities are combined to estimate the cooling time of the ambient gas (see § 8.3), which suggests that many of these gaseous environments may have cooling flow cores.

As noted above, the ambient gas temperatures increase systematically with redshift. This could either be due to a systematic error in the velocity estimates or be associated with the flux-limited sample. The radio power increases strongly with redshift for the flux-limited sample studied, and the velocity increases with radio power, which may cause a preferential detection of sources in high-temperature regions at high redshift. It could also be that assumptions that go into the aging analysis break down at high redshift. For example, it is assumed that the hot spot spectral index is the initial spectral index and that it is a power law. Perhaps the injection index is curved rather than a power law, or perhaps inverse Compton and synchrotron aging are so large at high redshift that the observed spectral index has already been affected by cooling and thus is not the injection index.

It is interesting to note that the radio data corrected for the correlation between the injection radio spectral index and the redshift yield temperatures that do not show a statistically significant increase with redshift when a fit allowing the temperature to vary with both core-lobe separation and redshift is considered. This may imply that using raw injection spectral indices, which increase strongly with redshift, yields velocity estimates that are systematically high at high redshift, and that the injection spectral indices should be corrected to zero redshift.

Wan & Daly (1997) are testing these and other hypotheses. One test will be to compare two estimates of the ambient gas pressure. For example, the bridge pressure at the break can be estimated using the bridge magnetic field strength at that point, and can be compared with the thermal pressure of the ambient gas estimated using the density and temperature estimates presented here and by WDW97. If the increase in the temperature with redshift is due to a systematic error in the velocity, then these two pressure estimates should diverge with redshift. If the power selection effect causes higher temperature regions to be detected at high redshift, the ratio of the two pressure estimates should be redshift-independent. This analysis is ongoing.

The authors would like to thank Mitch Begelman, Roger Blandford, Renyue Cen, Dave De Young, George Djor-

govski, Ed Groth, Eddie Guerra, Tom Herbig, Jill Knapp, Paddy Leahy, Simon Lilly, Malcolm Longair, Alan Marscher, George Miley, Colin Norman, Jerry Ostriker, Lyman Page, Jim Peebles, Rick Perley, Tony Readhead, Martin Rees, Brigitte Rocca, David Schramm, Rashid Sunyaev, and David Wilkinson for helpful comments and discussions. Special thanks are extended to Robert Lupton for his assistance throughout the data analysis of this work, and to Guy Pooley for providing FITS images of the LPR92 sources. It

is a special pleasure to thank those involved with the Aspen Center for Physics, which provided a very stimulating environment for the presentation and discussion of this work. This work was supported in part by the US National Science Foundation, the Natural Sciences and Engineering Research Council of Canada, the Independent College Fund of New Jersey, and by a grant from W. M. Wheeler III.

## REFERENCES

- Alexander, P. 1987, *MNRAS*, 255, 27  
 Alexander, P., & Leahy, J. P. 1987, *MNRAS*, 225, 1  
 Allen, C. W. 1973, *Astrophysical Quantities* (London: Athlone)  
 Arnaud, K. A., Fabian, A. C., Eales, S. A., Jones, C., & Forman, W. 1984, *MNRAS*, 211, 981  
 Begelman, M. C., Blandford, R. D., & Rees, M. J. 1984, *Rev. Mod. Phys.*, 56, 255  
 Begelman, M. C., & Cioffi, D. F. 1989, *ApJ*, 345, L21  
 Blandford, R. D. 1996, in *Cygnus A Workshop*, ed. C. Carilli & D. Harris (Cambridge: Cambridge Univ. Press), 64  
 Carilli, C. L., Perley, R. A., Bartel, N., & Dreher, J. W. 1996, in *Cygnus A Workshop*, ed. C. Carilli & D. Harris (Cambridge: Cambridge Univ. Press), 76  
 Carilli, C. L., Perley, R. A., & Dreher, J. H. 1988, *ApJ*, 334, L73  
 Carilli, C. L., Perley, R. A., Dreher, J. W., & Leahy, J. P. 1991, *ApJ*, 383, 554  
 Carilli, C. L., Perley, R. A., & Harris, D. E. 1994, *MNRAS*, 270, 173  
 Daly, R. A. 1990, *ApJ*, 355, 416  
 ———. 1992, *ApJ*, 399, 426  
 ———. 1995, *ApJ*, 454, 580  
 Fernini, I., Burns, J. O., Bridle, A. H., & Perley, R. A. 1993, *AJ*, 105, 1690  
 Garrington, S. T., Conway, R. G., & Leahy, J. P. 1991, *MNRAS*, 250, 171  
 Jaffe, W. J., & Perola, G. C. 1973, *A&AS*, 26, 423  
 Laing, R. A. 1980, *MNRAS*, 193, 439  
 ———. 1981, *ApJ*, 248, 87  
 Leahy, J. P. 1991, in *Beams and Jets in Astrophysics*, ed. P. A. Hughes (Cambridge: Cambridge Univ. Press), 100  
 Leahy, J. P., Muxlow, T. W. B., & Stephens, P. W. 1989, *MNRAS*, 239, 401 (LMS89)  
 Leahy, J. P., & Williams, A. G. 1984, *MNRAS*, 210, 929  
 Liu, R., Pooley, G., & Riley, J. M. 1992, *MNRAS*, 257, 545 (LPR92)  
 Myers, S. T., & Spangler, S. R. 1985, *ApJ*, 291, 52  
 Moffet, A. T. 1975, in *Stars and Stellar Systems, IX: Galaxies and the Universe*, ed. A. Sandage, M. Sandage, & J. Kristan (Chicago: Univ. Chicago Press), 211  
 Neesser, M. J., Eales, S. A., Law-Green, J. D., Leahy, J. P., & Rawlings, S. 1995, *ApJ*, 451, 76  
 Pacholczyk, A. G. 1970, *Radio Astrophysics* (San Francisco: Freeman)  
 Perley, R. A., & Carilli, C. L. 1996, in *Cygnus A Workshop*, ed. C. Carilli & D. Harris (Cambridge: Cambridge Univ. Press), 168  
 Perley, R. A., & Taylor, G. B. 1991, *AJ*, 101, 1623  
 Reynolds, C. S., & Fabian A. C. 1996, *MNRAS*, 278, 479  
 Rybicki, G. B., & Lightman, A. P. 1979, *Radiative Processes in Astrophysics* (New York: Wiley)  
 Scheuer, P. A. G. 1995, *MNRAS*, 277, 331  
 ———. 1996, in *ASP Conf. Ser. 100, Energy Transport in Radio Galaxies and Quasars*, ed. P. E. Hardee, A. H. Bridle, & J. A. Zensus (San Francisco: ASP), 333  
 Wan, L., & Daly, R. A. 1997, in preparation  
 Wellman, G. F. 1997, Ph.D. thesis, Princeton Univ., in preparation  
 Wellman, G. F., & Daly, R. A. 1996a, in *Cygnus A Workshop*, ed. C. Carilli & D. Harris (Cambridge: Cambridge Univ. Press), 215  
 ———. 1996b, in *Cygnus A Workshop*, ed. C. Carilli & D. Harris (Cambridge: Cambridge Univ. Press), 240  
 Wellman, G. F., Daly, R. A., & Wan, L. 1997, *ApJ*, 480, 96 (WDW97)